Determining maximum entropy in 3D remote sensing height distributions and using it to improve aboveground biomass modelling via stratification

Adnan, Syed; Maltamo, Matti; Mehtätalo, Lauri; Ammaturo, Rhei N.L.; Packalen, Petteri; Valbuena, Rubén

Remote Sensing of Environment

DOI:
10.1016/j.rse.2021.112464

Published: 01/07/2021

Peer reviewed version

Title:

Determining maximum entropy in 3D remote sensing height distributions and using it to improve aboveground biomass modelling via stratification.

Authors:

Syed Adnan*(1), Matti Maltamo (1), Lauri Mehtätalo (2), Rhei N. L. Ammaturo (3), Petteri Packalen (1), Rubén Valbuena*(4)

Affiliations:

(1) University of Eastern Finland, School of Forest Sciences. PO Box 111. FI-80101. Joensuu, Finland. adnan@uef.fi; matti.maltamo@uef.fi; petteri.packalen@uef.fi

(2) University of Eastern Finland, School of Computing, P.O. Box 111, FI-80101 Joensuu, Finland. lauri.mehtatalo@uef.fi

(3) University of Cambridge, Department of Plant Sciences, Forest Ecology and Conservation, Downing Street, CB2 3EA Cambridge, UK. nla32@cam.ac.uk

(4) Bangor University. School of Natural Sciences, Thoday building. Bangor. Gwynedd, LL57 2UW. UK. r.valbuena@bangor.ac.uk

*Corresponding authors.

Keywords

forest structure, forest aboveground biomass, Gini Coefficient, L-moments, airborne laser scanning

Abstract

McArthur's foliage height diversity (FHD) has been the gold standard in the determination of structural complexity of forests characterized by LiDAR vertical height profiles. It is based on Shannon's entropy index, which was originally designed to describe evenness in abundances among qualitative typologies, and thus the calculation of FHD involves subjective layering steps which are essentially unnatural to describe a continuous variable (X) such as height. In this contribution we aim to provide a mathematical framework for determining maximum entropy in 3D remote sensing datasets based on the Gini Coefficient of theoretical continuous distributions, intended to replace FHD as entropy measure in vertical profiles of LiDAR heights (1D; X), with extensions to variables expressing dimensions of higher order (2D or 3D, $Z \propto X^2$ or X^3). Then we apply this framework to Boreal forests in Finland to describe landscape heterogeneity with the intention to improve the modelling of forest aboveground biomass (AGB), hypothesizing that LiDAR models of AGB should essentially be different in areas of differing structural characteristics. We carried out a pre-stratification of LiDAR data collected in 2012 using simple rules applied to the L-skewness (L_{skew}) and L-coefficient of variation of LiDAR echo heights (L_{cv}; equivalent to the Gini coefficient, GC_H), determining a new threshold at $GC_H = 0.33$ as a consequence of the newly developed mathematical proofs. We observed only moderate improvements in terms of model accuracies: RMSDs reduced from 41.7% to 38.9 or 37.0%. More remarkably, we identified critical differences in the metrics selected at each stratum, which is useful to understand what predictor variables are more important for estimating AGB at each area of a forest. We observed that higher LiDAR height percentiles are more relevant at open canopies and heterogeneous forests, whereas closed canopies in homogeneous forests obtain most accurate predictions from a combination of cover metrics and percentiles around the median. Without stratification, the overall model would neglect explained variability in the structural types of lower occurrence, and predictions from

51 a model influenced by structural types of higher occurrence would be biased at those areas.
52 These results are thus useful in terms of improving our understanding on the relationships
53 underlying LiDAR-AGB models.
54
55 **1. Introduction**
56 Structural complexity is an essential morphological trait of ecosystems, complementary to
57 others like vegetation height or cover (Schneider et al. 2017; Fahey et al. 2019; Valbuena et al.
58 2020), which is relevant to various ecological processes such as nutrients cycling, carbon
59 sequestration and species interactions (Brokaw and Lent 1999; Lindenmayer et al. 2000;
60 McElhinny et al. 2005). There is however a lack of consensus on the most appropriate means
61 to measure the structural complexity of ecosystems (Neumann and Starlinger 2001; Lexerød
62 and Eid 2006), with approaches focused on measuring either entropy, e.g. Simpson or Shannon
63 indices (McArthur and McArthur 1961), or variability, e.g. variance or Gini coefficient (GC)
64 (Weiner 1990). The most popular approach follows the early works of McArthur and McArthur
65 (1961) who calculated the Shannon-based foliage height diversity (FHD) after layering the
66 ecosystem vertical profile into three strata, but there have been pleas for alternative measures
67 (Lovejoy 1972; Pearson 1975; Erdelen 1984; Weiner and Thomas, 1986; Valbuena et al. 2012).
68 This dichotomy has been reflected in the derivation of structural complexity measures from
69 LiDAR, with alternatives based on either layering the vertical profile (Lefsky et al. 2002a;
70 Vierling et al. 2008; Simonson et al. 2014; Weisberg et al. 2014; Listopad et al. 2015; Wilkes
71 et al. 2016; Almeida et al. 2019a; Bakx et al. 2019) or measuring variability in LiDAR heights
72 (Valbuena et al. 2017a; Moran et al. 2018; Mononen et al. 2019; Crespo-Peremarch et al. 2020;
73 Hagar et al. 2020).

74 In this contribution we propose a mathematical framework (**Appendix A**) which effectively
75 merges both approaches, by showing how maximum entropy can be flagged up from values of

76 a variability measure such as the Gini coefficient. They constitute formal deductive proofs of
77 ideas that have previously been presented on the basis of empirical indications: such as a
78 threshold at $GC = 0.5$ employed to discriminate ecosystem structural heterogeneity (Valbuena
79 et al. 2012, 2017a). Based on these mathematical developments, we further argue that different
80 thresholds apply for GC depending on whether calculated from LiDAR heights (GC_H), or tree
81 basal areas (GC_{BA}), because the former is a variable representing one dimension (X) and the
82 latter is an area, and thus bi-dimensional (X^2) (**Appendix A**). This mathematical framework
83 thus provides unified means for determining maximum entropy in the 3D space of information
84 provided by remote sensing tools such as LiDAR.

85 To quantify the amount of carbon sequestered by forests over large geographical areas, and use
86 them to inform global policies, it is important to attain reliable estimations of forest
87 aboveground biomass (AGB) from local to global scales (Gibbs et al. 2007). In this context,
88 remote sensing in general, and LiDAR in particular, are the key technologies to monitor
89 reductions in emissions of greenhouse gases from deforestation and forest degradation (REDD)
90 (Boudreau et al. 2008; Asner et al. 2010). Airborne LiDAR produces detailed canopy
91 information (Maltamo et al. 2005; Gobakken and Næsset 2008) that provides opportunities for
92 predicting accurately various ecosystem attributes such as vegetation height (Magnussen et al.
93 1999; Maltamo et al. 2004; Koukoulas and Blackburn, 2005), tree diameters (Næsset, 2002;
94 Räty et al. 2018), structural heterogeneity (Vierling et al. 2008; Weisberg et al. 2014; Adnan
95 et al. 2019), tree species (Van Aardt et al. 2008), or forest biomass and carbon (Næsset and
96 Gobakken 2008; Kronseder et al. 2012; Valbuena et al. 2017b). Metrics derived from airborne
97 LiDAR are the most promising information for efficient and accurate AGB prediction (Asner
98 and Mascaro 2014; Bouvier et al. 2015; Longo et al. 2017). For this reason, these metrics are
99 employed as auxiliary variables in airborne LiDAR-assisted estimations (Gobakken and
100 Næsset 2008; Asner et al. 2010). Mehtätalo and Nyblom (2009, 2012) developed the

relationship between canopy height obtained from airborne LiDAR data and forest attributes such as stand density and mean tree height, improving model-based estimations. However, we still lack information on the relationship between LiDAR metrics with the forest AGB, and how the predictive models are affected by forest structures (Drake et al. 2003; Knapp et al. 2020).

Researchers have developed a wide variety of LiDAR models estimating AGB stocked in forests (Zolkos et al. 2013). The prediction error of the total AGB is dependent on the relationship between foliage observed by LiDAR and various AGB components (Lefsky et al. 2002b; Næsset and Gobakken 2008; Hernando et al. 2019). Thus, high heterogeneity in the structural complexity of forests may cause difficulties in modelling (Drake et al. 2003; Hall et al. 2005; Jaskierniak et al. 2011; Vincent et al. 2014). While there have been many attempts to generalize LiDAR modelling of AGB (Asner and Mascaro 2014; Bouvier et al. 2015), a general relationship may not be appropriate for all regions, both even and uneven sized forests or dense and sparse spatial structures (Vincent et al. 2014; Häbel et al. 2019; Knapp et al. 2020). To overcome this difficulty, the forest area can be stratified into different development classes (Næsset 2002) or forest structural types (FSTs) (Mascaro et al. 2011; Vincent et al. 2014), and a separate model can be applied to each of them to obtain more reliable AGB estimations. With these regards, we hypothesised that the Gini coefficient can be useful for such FST stratification prior to modelling the forest AGB. Bollandsås and Næsset (2007) obtained reliable results following such approach with the support of field information (i.e., GC_{BA}). Alternatively, we postulated that these FSTs could be detected directly from airborne LiDAR data (i.e. GC_H), and apply a separate AGB model in each FST to improve AGB predictions. Based on results in Valbuena et al. (2017a), we considered the use of L-moment ratios for such stratifications: L-coefficient of variation of LiDAR echo heights (L_{cv}; equivalent to the Gini coefficient, GC_H) and L-skewness (L_{skew}). We considered a new threshold at $GC_H = 0.33$ for separating even sized from uneven sized forest structures, based on findings in **Appendix A**. Furthermore,

126 Valbuena et al. (2017a) also identified FSTs according to their light environment characteristics
127 using the $L_{skew} = 0$ threshold which segregate the euphotic/open canopy and
128 oligophotic/closed canopy forest areas (Lefsky et al. 2002a), by separating them as positive
129 and negative skewness in between the [-1,1] bounds of L_{skew}. We evaluated the potential of
130 these detected FSTs in improving the AGB prediction from the airborne LiDAR data.

131 In this article, we set the mathematical foundations for determining maximum entropy from a
132 distribution of heights in 3D remote sensing (**Appendix A**), as an alternatively to common
133 binning procedures employed to determine McArthur and McArthur's (1961) FHD. Then we
134 employed this rationale, stratified the LiDAR-surveyed area according to the $L_{cv} = 0.33$ and
135 $L_{skew} = 0$ rules following Valbuena et al. (2017a), and carried out stratified sampling with
136 roughly equal sample sizes within each FST. The aim of this stratification was to evaluate the
137 potential of FSTs to improve forest AGB predictions in the pre-stratified airborne LiDAR data
138 compared to the AGB predictions in the whole dataset without pre-stratification. We developed
139 a general LiDAR-AGB model for the whole dataset without pre-stratification, and separate
140 FST-specific models at each stratum. We hypothesized that LiDAR models predicting AGB
141 should essentially be different in areas of differing structural characteristics. For this reason,
142 we also paid careful attention to the LiDAR metrics selected at each model, and used those
143 results to make inferences on the relationship behind the choice of metrics at each forest area,
144 with the intention to shed light on the effects of forest heterogeneity on LiDAR models
145 predicting AGB.

146 **2. Material and Methods**

147 *2.1. Study Area and data collection*

148 This study was conducted in a 252,000 ha boreal forest located in the North Karelia region of
149 Finland (Figure 1). The dominant species in the study area are Norway spruce (*Picea abies* (L.)

150 Karst.), Scots pine (*Pinus sylvestris* L.) and Birch species (*Betula* spp.), and some other
151 deciduous species such as *Alnus* spp. and *Populus* spp. are also present. In May 2012, a Leica
152 ALS60 laser scanning system was used to collect airborne LiDAR data. Flight elevation was
153 2,300 m above ground level, which resulted in a scan density of 0.91 pulses per square meter.
154 The digital terrain model with 2 m resolution derived from the same LiDAR dataset was
155 provided by National Land Survey (Finland). The DTM was subtracted from the LiDAR echo
156 heights and area-based LiDAR metrics were computed using the FUSION software (Version
157 3.70, USDA Forest Service; McGaughey 2019). With the intention to get in the full structural
158 characteristics of forests and commensurate with forest data acquisition, a very small height
159 threshold (< 0.1 m) was used to exclude ground echoes in the computation of area-based
160 metrics (Görgens et al. 2017). This eliminates ground echoes but consider seedlings and
161 saplings, which were included in the field inventory (Valbuena et al. 2016). Among the set of
162 FUSION metrics, two L-moment ratios were used for simulating a pre-stratification: L-
163 coefficient of variation (L_{cv}) and L-skewness (L_{skew}). The remaining metrics were involved in
164 the modelling of AGB.

165 ****approximate position of Figure 1*****

166 Field data for the calibration/validation of AGB models were jointly collected by the Finnish
167 Forest Centre (Suomen Metsäkeskus; SMK) and University of Eastern Finland (UEF) in 2013
168 (Valbuena et al. 2017a). There were 244 field plots in total from eight different strata and
169 sample size was approximately equal in each stratum. The stratification was based on the forest
170 development classes – seedling, sapling, young, advanced, mature, shelterwood, seed-tree and
171 multi-storey (Valbuena et al. 2016) –, determined on the basis of the SMK stand-wise
172 information from the previous forest management plan, randomly selecting plot locations over
173 areas covering each development class. Field data acquisition consisted in a concentric circle

174 design, recording species and diameter at breast height (dbh; cm) of trees within each
175 concentric plot according to its size (Valbuena et al. 2016). Tree heights (h; m) were measured
176 only for the basal area median tree of each species. For the even sized development classes
177 (young, advanced and mature), the field data were collected by SMK using a plot size of 9 m
178 radius for trees with $dbh > 8$ cm, while saplings were recorded within 5.64 m radius and
179 seedlings were counted using a 2.82 m long stick in distributed sub-plots (Figure 2). Plots
180 within the seed tree, shelterwood and multi-storey development classes were collected by UEF
181 using the same plot design. However, the size of the outer plot in these three development
182 classes was slightly increased to 9.77 m so that its size would become integer multiplier of the
183 inner subplots, which is convenient for the calculation of GC_{BA} following Valbuena et al.
184 (2013). For visual comparison of these development classes, mean leaf area density (LAD)
185 vertical profiles with 95% confidence intervals from all plots within each development class
186 were calculated from LiDAR data using the R package *LeafR* (Almeida et al. 2019b).

187 ****approximate position of Figure 2*****

188 *2.2 Rule-based stratification of forest structural types using airborne lidar data*

189 Postulating that LIDAR models of AGB should be essentially different in areas of differing
190 structural characteristics, we employed this dataset to simulate a pre-stratification scenario by
191 classifying the prediction area into FSTs detected directly from the LiDAR data. The study
192 area was stratified using the abovementioned two L-moment ratios of airborne LiDAR height
193 distributions, and the rules were deduced from their mathematical properties instead of
194 inductive statistical distributions or supervised classification, thus absence of any field
195 information is involved (Valbuena et al. 2016). As L_{cv} is mathematically equivalent to the Gini
196 coefficient of LiDAR echo heights (GC_H) (Valbuena et al. 2017a), it could be used to describe
197 the structural properties related to the inequality in tree sizes within a forest area. $L_{cv} =$

198 0.33 was used as a boundary line to discriminate forests with even-sized FSTs ($L_{cv} < 0.33$)
199 from uneven-sized ones ($L_{cv} > 0.33$), on the grounds that maximum entropy in the distribution
200 of LiDAR heights is reached at $L_{cv} = 0.33$ (**Appendix A**). Similarly, asymmetry (L_{skew})
201 describes the structural heterogeneity related to light availability and tree size dominance
202 (Valbuena et al. 2017a). $L_{skew} = 0$, which represents the symmetric distribution of LiDAR
203 echo heights, was used to separate forests having oligophotic areas/closed canopy ($L_{skew} < 0$)
204 from euphotic areas/open canopy areas ($L_{skew} > 0$) (Lefsky et al. 2002a).

205 *2.3 Aboveground biomass calculation from field data*

206 R statistical software (R Core Team 2019) was used for all statistical analyses and modelling.
207 Locally developed species-specific biomass equations were used to calculate tree above-
208 ground biomass (agb; kg) for Scots pine and Norway spruce (Repola, 2009), and another for
209 birch (Repola, 2008) which was used for all deciduous species. These were based on dbh and
210 h, and thus individual tree heights were subsequently predicted using the Näslund's height
211 curve (1936):

212 $$h = 1.3 + \left(\frac{dhb}{\beta_0 + \beta_1 dbh}\right)^{\alpha}, \quad (1)$$

213 where the exponent was $\alpha = 2$ for pine and deciduous species, and $\alpha = 3$ for spruce. We
214 followed the methods suggested by Siipilehto (1999) in the estimation the Näslund's height
215 curve model parameters (β_0, β_1) for each species. which included plot-level calibration with
216 species-specific diameter ($D_{\widetilde{ba}}$) and height ($H_{\widetilde{ba}}$) of the tree with median basal area ($\widetilde{ba}$). Then
217 the species-specific parameters were used in the height curve model to predict the missing tree
218 heights from their dbh. Once calculated all the tree level agb values, they were aggregated to
219 plot level (AGB; Mg·ha^{-1}) according to their corresponding hectare expansion factors, and used
220 as a response variable in subsequent LiDAR models.

221 *2.4 Modelling of aboveground biomass from airborne LiDAR data*

222 Many airborne LiDAR derived metrics (predictors) were available for modelling the AGB. We
223 used function "*regsubset*" of the R package "*leaps*" (Lumley and Miller, 2017), which
224 performed a selection of the best subset of predictors using an exhaustive search among typical
225 LiDAR-AGB models (Valbuena et al. 2017b). We made an independent selection, the best
226 subset of predictors for the general model including the whole dataset (i.e. without
227 stratification), and also for each FST-specific model (even versus uneven sized forest
228 structures, and euphotic/open canopy versus oligophotic/closed canopy areas). Thereafter,
229 modelling based on the k-nearest neighbour (k-NN) method was used to predict the response
230 variable (AGB) from the best subset of airborne LiDAR predictors (Mcinerney et al. 2010). We
231 used Euclidean distance with $k = 5$ in the k-NN implementation available in the R package
232 "*YaImpute*" (1.0-31 version; Crookston and Finley, 2008).

233 *2.5 Accuracy assessment of aboveground biomass prediction*

234 We used a 10-fold cross validation method for assessing the accuracy of the resulting models.
235 The results of the general model and FST-specific models were evaluated and compared by
236 means of their mean difference (MD) and root mean square difference ($RMSD$):

237 $$RMSD = \sqrt{\frac{\sum_{i=1}^{n}((y_i{}^{cv} - \hat{y}_i)^2}{n}}, \quad (2)$$

238 $$MD = \frac{\sum_{i=1}^{n}((y_i{}^{cv} - \hat{y}_i)}{n}, \quad (3)$$

239 where n is the total number of observations (field plots), $y_i{}^{cv}$ and $\hat{y}_i$ are the predicted and
240 observed value of AGB for observation i, respectively. Relative values (%) of MD and $RMSD$
241 were obtained as the percentage over the mean observed AGB. As an additional quality control
242 measure, we used a hypothesis test on the 1:1 correspondence between the observed (obs_i) and

predicted ($pre_i{}^{cv}$) values from the intercept (α) and slope (β) of their linear regression (Leite and Oliveira, 2002; Piñeiro et al. 2008),

$$obs_i = \alpha + \beta pre_i{}^{cv}, \quad (4)$$

To avoid overfitting the models to the sample, the best subset procedure was constrained by additional restrictions to the sum of squares ratio (SSR), which evaluates the inflation in the unexplained variance when the model is not cross-validated (Valbuena et al. 2017b). SSR is the ratio between the squared root sum of the squares obtained by cross validation (SS^{cv}) and without cross validation (SS^{fit}).

$$SSR = \sqrt{SS^{cv}}/\sqrt{SS^{fit}}, \quad (5)$$

$$SS^{cv} = \sum_{i=1}^{n}(y_i{}^{cv} - \hat{y}_i)^2 \quad (6)$$

$$SS^{fit} = \sum_{i=1}^{n}(y_i{}^{fit} - \hat{y}_i)^2 \quad (7)$$

Where, $\hat{y}_i$ is the observed value of the AGB for observation i, and $y_i{}^{cv}$ and $y_i{}^{fit}$ are the predicted values using cross validation and without cross validation, respectively.

3. Results

3.1. Airborne LiDAR based forest structural types

Table 1 gives a development class-wise summary of plot-level characteristics calculated from the field data – density (N), quadratic mean diameter (QMD), above ground biomass density (AGB) and Gini coefficient of basal area (GC_{BA}) –, and also from the LiDAR data – L-coefficient of variation (L_{cv}; equivalent to the Gini coefficient, GC_H) and L-skewness (L_{skew}). of LiDAR return heights –. Height profiles of each development class calculated from LiDAR data are given in **Figure 3**, which shows mean changes in LAD through the vertical profiles at each development class. **Figure 4** further shows how different forest structural types detected

directly from airborne LiDAR data are distributed either sides of the $L_{cv}(GC_H) = 0.33$ and $L_{skew} = 0$ thresholds. Some structural dynamics can be observed from these figures, since the majority of areas in seedling development classes were separated as even sized by $L_{cv}(GC_H) < 0.33$, because they are very small and roughly equal in size at first, to later more inequality in diameter distribution toward the sapling stage ($L_{cv}(GC_H) > 0.33$) (**Figure 4a**). Likewise, the young, advanced and mature development classes which mostly contain equality in diameter/basal area distribution were mostly separated as even sized ($L_{cv}(GC_H) < 0.33$). Seed trees and multi-storied development classes have higher inequality in their diameter distribution, they show high dispersion in their LiDAR echoes, and thus they were separated as uneven sized structure ($L_{cv}(GC_H) > 0.33$). Similarly, in **Figure 4b** most seedling and sapling development classes were separated as euphotic areas ($L_{skew} > 0$) because their canopies have not closed yet at these stages of development. As they grow and increase in AGB through young, advanced and mature development classes, they shift toward oligophotic areas with closed canopies and negative skewness of LiDAR return heights ($L_{skew} < 0$). The shelterwood development class which has a dense overstory and high LiDAR returns was classified as oligophotic ($L_{skew} < 0$), whereas seed-tree areas and multi-storey development classes with sparse overstorey were mainly classified as euphotic ($L_{skew} > 0$).

****approximate position of Table 1*****

****approximate position of Figure 3*****

****approximate position of Figure 4*****

We were then interested on whether the different thresholds that **Appendix A** shows for LiDAR heights ($GC_H(L_{cv}) = 0.33$) and field data ($GC_{BA} = 0.5$) would segregate forests with similar structural properties. **Figure 5** shows a comparison of aggregated diameter distributions (plus basal area-weighted distributions, in darker colors in the background) with confidence

intervals. The difference between the distribution of proportions in density of stems versus basal area highlights structural differences which cannot be easily appreciated in diameter distributions, since in highly complex structures with large differences in tree sizes the proportion of basal area taken by larger trees becomes predominant. This could be appreciated in the distributions of strata yielded from the LiDAR data only ($GC_H(L_{cv}) < 0.33$ and $GC_H(L_{cv}) > 0.33$, respectively in **Figures 5a** and **b**), as much as it was for the distributions yielded when the strata was generated using the field data itself ($GC_{BA} < 0.50$ and $GC_{BA} > 0.50$, respectively in **Figures 5c** and **d**). These results emphasize the reliability of a purely LiDAR-based classification in the structural heterogeneity assessment of forests.

****approximate position of Figure 5****

3.3. Best-subset variable selection

In order to facilitate direct comparison of all models, we fixed the number of LiDAR predictors to be six for all models, based on the SSR restriction of the best-subset procedure which assured that none of them had over-fitting effects, plus a positive outcome in the hypothesis test of 1:1 correspondence. **Table 2** shows the variables selected at each of them: the general model developed for the whole data without pre-stratification, and each FST-specific model developed for the even and uneven sized forest structures and oligophotic/closed canopy and euphotic/open canopy areas, obtained from the direct classification of airborne LiDAR data. While all the selected predictors were those typically included in LiDAR-AGB modelling – averages (e.g. quadratic or cubic means), dispersion statistics (e.g., variance), percentiles, and cover metrics (i.e. percentages above thresholds) of LiDAR return heights –, we identified critical differences in the metrics selected at each stratum, which is useful to understand what predictor variables are more important for estimating AGB at each area of a forest. We observed that higher LiDAR height percentiles were more relevant at open canopies and heterogeneous

forests, whereas closed canopies in homogeneous forests obtained a best subset based on combinations of cover metrics and percentiles around the median. In the uneven-sized structures, higher percentiles, variance and absolute average deviation of LiDAR return heights were selected. On the other hand, in the even-sized stratum the model included the mode, L_{skew}, the median, and cover metrics (percentage of all returns above mode and total first returns). Similarly, in the oligophotic/closed canopy areas, the median and cover metrics were important, while in the euphotic areas/open canopy areas, higher percentiles and mean absolute deviation from median and variance were selected. Thus, the similarities of even-sized with oligophotic areas on one hand, and uneven with euphotic areas observed in **Figure 4**, showed an influence in the modelling itself (**Table 2**), thus indicating convergence in the relationships between structure and modelling results.

****approximate position of Table 2****

3.3. Modelling aboveground biomass from airborne LiDAR based forest structural types

The AGB was predicted in each model using the associated best subset of LiDAR predictors, and their accuracies were assessed. In the general model (**Table 3** and **Figure 6**), i.e. a model fitted using the whole dataset, the RMSD between the observed and predicted AGB was 37.4 Mg·ha^{-1}. We disaggregated these accuracy statistics by strata, to allow direct comparison with the FST-specific models, which resulted in 37.1 and 37.6 Mg·ha^{-1} respectively in the even and uneven-sized forest areas and resulted in 37.6 and 37.3 Mg·ha^{-1} in oligophotic and euphotic areas, respectively. In relative terms, the general model RMSD 41.7%, which seems high because of the inclusions of seedling and sapling areas of very low AGB in the dataset. The general model showed some bias when applied to specific FSTs, as it can be appreciated by underpredictions of around 4.8-5.5% in terms of their MDs, with the even-sized forests being the only areas where not such strong bias effect was observed (-2.33% only).

337 ****approximate position of Table 3*****

338 ****approximate position of Figure 6*****

339 The results for the FTS-specific models are summarized in **Tables 4a-b**, and the scatterplots in
340 **Figures 7-8**. The RMSD improved both in the even sized (34.6 $Mg \cdot ha^{-1}$) and uneven sized
341 (35.3 $Mg \cdot ha^{-1}$) forest structures (**Table 4a**) as compared to the general model (**Table 3**). The
342 MD similarly improved in the uneven sized forest structure (-2.72 $Mg \cdot ha^{-1}$) and only slightly
343 decreased in the even sized areas (-2.30 $Mg \cdot ha^{-1}$). These specific models developed for the even
344 and uneven sized forest structures also showed an improvement in the MD and RMSD when
345 aggregated for the whole area (-2.52 and 34.9 $Mg \cdot ha^{-1}$) (**Table 4a**), compared to the general
346 model (-3.55 and 37.4 $Mg \cdot ha^{-1}$) (**Table 3**). Similar improvements in the MD and RMSD were
347 observed in the FST specific models developed for the oligophotic/closed canopy areas (-2.22,
348 33.5 $Mg \cdot ha^{-1}$), euphotic areas/open canopies (-2.52, 32.9 $Mg \cdot ha^{-1}$), and whole data (-2.37, 33.2
349 $Mg \cdot ha^{-1}$) (**Table 4b**). All the FST-specific modelling approaches, thus, showed improvements
350 compared to the general model both in terms of unbiasedness and improving the precision of
351 predictions.

352 ****approximate position of Table 4*****

353 ****approximate position of Figure 7*****

354 ****approximate position of Figure 8*****

355 **4. Discussion**

356 *4.1. Determining maximum entropy from a distribution of heights in 3D remote sensing*

357 In previous contributions we have showed a threshold of interest which flags up maximum
358 entropy at the Gini Coefficient value of $GC_{BA} = 0.50$ (Valbuena et al. 2012, 2017). This

threshold allows to compare the entropy of the ecosystem using a statistic of dispersion, arguing that is more correct for continuous variables because it avoids the factitious binning step required when computing foliage height diversity (McArthur and McArthur, 1961), based on Shannon's entropy index which was originally meant for discrete variables (Shannon, 1948). It is important to note that this threshold is applicable for a Gini coefficient of a Lorenz curve representing differences in basal area among trees growing within a given area (GC_{BA}) (Valbuena et al. 2012). On the other hand, in this contribution we further argue that for a Gini coefficient of a Lorenz curve representing differences in LiDAR heights within that same area (GC_H), the alternative value of $GC_H = 0.33$ should be the one used instead to identify maximum entropy. The reason is that height is a one-dimensional variable (X), whereas basal areas are two-dimensional (X^2). In order to achieve these generalized conclusions, we need to use theoretical distribution functions and show how their parameters propagate into Lorenz curves and values of the Gini Coefficient directly dependent on those parameters. In the **Appendix A**, we show formal proofs for these values obtained from theoretical distributions, to illustrate the reasoning employed in this contribution. We also show how these maxim entropy values of GC_X extend to higher dimensions (e.g. GC_{X^2}), thus developing a mathematical framework which provides unified means for determining maximum entropy in the 3D space of information provided by remote sensing tools such as LiDAR. **Figure 5** illustrates empirically the equivalence of the LiDAR and field approaches.

4.2. Rule-based pre-stratification into different forest structural types

Airborne LiDAR explains the key characteristics of forests related to the structural heterogeneity that can be relevant to describe tree size hierarchy (Valbuena et al. 2013), vegetation growth (Stark et al. 2012) and light availability (Lefsky et al. 2002a). Advancement in airborne LiDAR remote sensing promises reliable accuracies in the prediction of biophysical

383 stand properties (Lefsky et al. 2002b; Valbuena et al. 2020) and various studies have evaluated
384 and found that the pre-stratification of forests using airborne LiDAR can improve the attribute
385 estimation (Næsset 2002; Maltamo et al. 2015) and reduce the sampling efforts (Papa et al.
386 2020). Following the same concept but using solely the LIDAR data as opposed to using field
387 information, in this study different FST were obtained from the direct classification of airborne
388 LiDAR data. We applied rule-based pre-stratifications and used $L_{cv}(GC_H)$ and L_{skew} of the
389 LiDAR echo heights which are the two prominent LiDAR metrics in separating the even from
390 uneven sized structures and oligophotic/closed canopy from euphotic/open canopy forest areas,
391 respectively (Valbuena et al. 2017a). In **Figure 4a**, we found that the young, advanced and
392 mature development classes which have similar diameters and basal areas distributions
393 ($GC_{BA} < 0.5$) usually backscatter most of the LiDAR returns and hold smaller variance in their
394 height values were mostly separated by the lower values of $L_{cv}(GC_H) < 0.33$. There is a
395 consistency on results in **Table 1** showing that LiDAR values of GC_H are reflected by higher
396 values in GC_{BA}, with the proofs in **Appendix A** being the explanation for this effect. A notable
397 exception is observed in the case of the sapling development, which showed a high uncertainty
398 in terms of GC, with a wide range of values in both GC_{BA} and GC_H (**Table 1**). This is the reason
399 that L_{skew} was important to add as an additional LiDAR metric because the similarity between
400 GC_{BA} (Valbuena et al. 2013) and GC_H (L_{cv}) only occurs if the higher values of GC is due to the
401 presence of canopy gaps which allow large a portion of laser pulses to pass and disperse in the
402 canopy (Stark et al. 2012, Valbuena et al. 2017a). Thus, by looking at the L_{skew} values, the
403 sapling was separated as euphotic/open canopy areas ($L_{skew} > 0$) which could be the reason
404 of the higher L_{cv} values. Other development classes such as seed-tree and multi-storey areas
405 were separated as even sized by both GC_{BA} (0.73 and 0.92) and GC_H ($L_{cv} = 0.58$ and 0.58),
406 however, the shelterwood development class wherein the mean GC_{BA} was 0.95 was not
407 properly separated and many plots were below $L_{cv}(GC_H) = 0.33$ (**Figure 4** and **Table 1**). This

might be due to the omission of the understory vegetation by the lower point density of the ALS data in our study area (0.91 points.m^{-2}) and any pointy density lower than at least 3 points.m^{-2} are unsuitable for the structural heterogeneity assessment, using the GC in particular (Adnan et al. 2017). Thus, the disintegration of such classes could further be improved by increasing the pulse density of the LiDAR data (Gobakken and Næsset 2008; Ruiz et al. 2014).

When laser pulses hit a closed canopy vegetation, only a small portion of pulses penetrate the canopy, which is represented by LiDAR height distributions with negative asymmetry $L_{skew} < 0$. This also indicates the shady/oligophotic areas where only a smaller portion of light will reach the ground, for example, young, advance and mature development classes. Similarly, areas where smaller portion of LiDAR returns due to the presence of sparse vegetation denotes the open/euphotic areas which were detected by $L_{skew} > 0$, for example, seedlings, saplings, seed trees, shelterwood and multi-storey (**Figure 4b and Table 1**). **Figure 5** further highlights the importance of this rule-based classification and presents an adequate comparison between the even and uneven sized forest structures separated by the $GC_H(L_{cv}) = 0.33$, or $GC_{BA} = 0.5$ (**Appendix A**). In this figure, it is clear that the diameter and basal area weighted distributions in both even sized and uneven sized structure which are obtained from the GC_H (**Figure 5a and 5b**) and GC_{BA} (**Figure 5c and 5d**) are very similar and the small differences are due to missing detection of seedling in the smallest size class. This provides further insights that GC_H is an appropriate option to separate structural heterogeneity of forest.

4.3 Selection of best subsets of airborne LiDAR predictors in the AGB prediction models

Various alternatives are used to select the optimum number of parameters (predictors) to predict a response variable such as best subset, stepwise, and nearest neighbor (MSN) selection methods (Næsset et al. 2002; Van Aardt et al. 2008; Asner et al. 2010; Valbuena et al. 2017b, Almeida et al. 2019a). We used the best subset method which because the selection of a given

variable is independent of interactions among variables as they are selected (Hudak et al. 2006). Thus, the selection of the six predictors was independent from the other LiDAR metrics and the different modelling options, yet reaching several convergences. Minimizing the number of meaningful predictors that describe various aspects of the forest structures is an important consideration (Hudak et al. 2006, Asner and Mascaro 2014; Vincent et al. 2014; Bouvier et al., 2015; Valbuena et al. 2017b), and our selection of six predictors to allow model comparison (**Table 2**) was a compromise balance between model error and overfitting that worked well for all the options. The results obtained in variable selection are as valuable as the accuracy assessment itself, since it shows convergences between some areas of the forest and discrepancies between opposing FSTs. They also show which FSTs influence more the general model, with effects both in the overall error but also biasing effects in the areas of the forest that had a lower influence in the composition of the general model. Cover metrics were important in all model but more predominant in oligophotic areas. The variance of LiDAR return heights was only selected in the uneven sized structures and euphotic/open canopy areas. Different height percentiles were influential in different FST-specific models, with the median (50^{th} height percentile) being important in the even sized and oligophotic structures, and higher percentiles (70^{th} or 99^{th}, representing dominant trees) becoming selected in the uneven sized structure and euphotic areas (Adnan et al. 2017). Most importantly, the variables selected in the general model were highly influenced by the even-sized areas of the forest, with both models presenting large similarities (**Table 2**), which is a good explanation for the results observed in the accuracy assessment, since the general model showed lesser error in those areas and high levels of biasness in the remaining FSTs. All these demonstrate the superiority of obtaining FST-specific models to predict forest AGB from LiDAR, as opposed to approaches seeking a single model valid for all forest areas.

4.4 Comparison of the aboveground biomass predicted in the whole data without stratification and each pre-stratified FSTs

In addition to the typical statistics employed to evaluate the quality of AGB predictions, namely MD and $RMSD$ (Van Aardt et al. 2008; Kankare et al. 2013; Straub et al. 2013; Räty et al. 2018), we also employed an evaluation of the inflation of error in cross-validation (the SSR) and hypothesis test of 1:1 correspondence between observed and predicted AGB to enhance the reliability of our resulting models (Valbuena et al. 2017b). Considering the results obtained for whole dataset with either alternative, the 37.4 Mg·ha^{-1} $RMSD$ of the general model (**Table 3**), was improved by the FST-specific model approaches, reaching 34.9 Mg·ha^{-1} (**Table 4a**), and 33.2 Mg·ha^{-1} (**Table 4b**). Considering results obtained by FST, all figures also show improvements, even and even-sized areas where $RMSD$s improved from the 37.1 Mg·ha^{-1} (**Table 3**) to 34.6 Mg·ha^{-1} (**Table 4a**), with only a slight increase in MD. This is very important, as otherwise result in FST-wise MDs for the general model showed bias effects in forest areas highly structured. This is explained by the higher influence that even-sized areas had in the general model, possibly because LiDAR metrics have a larger explanatory capacity for AGB in these areas, thus showing potential harmful consequences in AGB modelling approaches neglecting the effects of forest structure. While the accuracies in AGB prediction improved only moderately in the FST-specific models as compared to the general model, the differences observed in the selection of airborne LiDAR predictors in each model can be critical, as they can produce biased results at specific areas of the forest. We thus encourage the prior classification into different FSTs for selecting the most relevant LiDAR predictors at each area of the forest, which besides of improving the estimation of AGB could provide important ecological insights on forest dynamics such as regeneration (Valbuena et al. 2013), self-thinning (Coomes and Allen, 2007) or productivity (Bourdier et al. 2016), and reduce the sampling efforts needed for a given level of accuracy (Papa et al. 2020), assisting in better

forest inventory, management and planning (Næsset 2002; Maltamo et al. 2015). Thus, the improved AGB prediction approach is suitable for purposes such as quantification of carbon stock for REDD activities for a large forest area, but also for a better forest management, planning and understanding of the natural dynamics within a large forest area.

5. Conclusions

Our results demonstrate the superiority of obtaining FST-specific models to predict forest AGB from LiDAR, as opposed to approaches seeking a single model valid for all forest areas. We recommend the use of LiDAR information to pre-stratify the forest area prior to the field campaign, so that forest data acquisition can be tailored to the structural characteristics of the area. In order to determine these structural characteristics, we defended the use of GC above the use of FHD, being less computationally demanding but also conceptually better. **Appendix A** provides a mathematical framework for determining maximum entropy in 3D remote sensing datasets based on the GC of theoretical continuous distributions, intended to replace FHD as entropy measure in one-dimensional LiDAR vertical profiles (1D), with extensions to higher order dimensions bi- or three-dimensional (2D or 3D).

Acknowledgements

Syed Adnan's PhD is funded by National University of Sciences and Technology (NUST), Pakistan under FDP 2014-15. Noemi L. Ammaturo worked at the Department of Plant Sciences supervised by Rubén Valbuena, under The Cambridge Earth System Sciences Doctoral Training Partnerships (Cambridge ESS DTP, reference NE/L002507/1), which is a scheme funded by the UK Natural Environment Research Council (NERC). We would like to thank the Editor-in-Chief, Associate Editor and three reviewers for their comments and suggestions for the manuscript.

Appendix A. Proofs for maximum entropy thresholds corresponding to $GC_X = 0.33$ and $GC_{X^2} = 0.50$.

Let X be a random variable taking values in the set of positive numbers, and $\mathrm{E}[X]$ its expectation. Let $f_X(x)$ and $F_X(x)$ be their probability density function (p.d.f.) and cumulative distribution function (c.d.f.), respectively, and further let $F_X^{-1}(p)$ be the quantile function (inverse of the c.d.f.; its generalized definition is $F_X^{-1}(p) = inf\{x: p \leq F(x)\}$). The Lorenz curve $L_X(p)$ specifies the accumulated proportion of the total of X that is attributed to a given accumulated share of the population ordered by increasing X. Thus, the Lorenz curve provides a mapping from interval [0,1] to interval [0,1], where the domain includes the proportion from the ordered population and the codomain the share of X. The Lorenz curve can be written as

$$L_X(p) = \frac{\int_0^p F^{-1}(t)dt}{\mathrm{E}[X]}, \text{ for } 0 \leq p \leq 1 \quad \text{(A.1)}$$

The Gini coefficient is the twice area between the Lorenz curve and the diagonal line $L_X(p) = p$, which is thus assessed with the integral:

$$GC_X = 1 - 2\int_0^1 L_X(p)\,dp \quad \text{(A.2)}$$

The Lorenz curve for aX for a positive constant a is the same as that of X. Therefore the Lorenz curve and Gini coefficient have the property of being invariant under linear scaling of X by a positive constant.

In applications using the distribution LiDAR heights $X = H$, the Lorenz curve $L_H(p)$ specifies the proportion of total accumulated heights at the $100p$ % of lower (or higher) vertical strata. In forest science, from the distribution of tree diameters $X = D$, the Lorenz curve $L_D(p)$ gives the proportion of total accumulated diameters for the $100p$ % smallest (or largest) trees. It is however more common to use variables which are logical to accumulate, such as basal area $X = BA$ or above-ground biomass $X = AGB$, as it is more useful to know the proportion of basal area or biomass accumulated from for the $100p$ % smallest (or largest) trees. These

529 variables are however never measured directly, and instead derived from a transformation of
530 D or H, or both (Mehtätalo and Lappi, 2020). The following proofs demonstrate: (1) the
531 threshold $GC_X = 0.33$ denotes maximum entropy for unidimensional measures, i.e. D or H;
532 and (2) that this value of maximum entropy for D derives into $GC_{X^2} = 0.50$ for the transformed
533 variable $Z = X^2$, namely the bi-dimensional measure BA, as it was empirically devised in
534 Valbuena et al. (2012).
535
536 *Proofs for the Lorenz curve and Gini Coefficient of a uniformly distributed variable*
537 *(maximum entropy)*
538 The continuous uniform distribution $U(x_{\max}, x_{\min})$ has equal probability density for any u-
539 length interval $[x, x+u]$ within the range $X \in [x_{\min}, x_{\max}]$. It has the maximum entropy
540 among all continuous distributions which have the same range (Sung and Bera, 2009). Thus,
541 for a given range $\theta = x_{\max} - x_{\min}$ and a given number of strata θ/u considered, the uniform
542 distribution yields the maximum value of Shannon's (1848) entropy index (Valbuena et al.
543 2012). In applications using LIDAR heights, this is a vertical profile showing even proportions
544 for all strata, yielding a maximum value for McArthur & McArthur's (1961) foliage height
545 diversity, with $x_{\min} = 0$ being the ground level and $x_{\max} = \theta$ being the maximum height of
546 vegetation.
547 The continuous uniform distribution $X \sim U(0, \theta)$ has the p.d.f.:

548 (A.3) $$f_X(x;\theta) = \begin{cases} 1/\theta, & \text{for } 0 \le x \le \theta \\ 0, & \text{otherwise} \end{cases}$$

549 The c.d.f. is:

550 (A.4) $$F_X(x;\theta) = \begin{cases} 0, \text{for } x < 0 \\ x/\theta, & \text{for } 0 \le x \le \theta \\ 1, & \text{for } \theta \le x \end{cases}$$

551 The quantile function and expected value are:

552 (A.5) $F_X^{-1}(p) = \theta p$

553 (A.6) $E[X](= \mu) = \frac{\theta}{2}$

554 Substituting these in Eq. (A.1), the Lorenz curve becomes (Figure A.1):

555 (A.7) $L_X(p) = \frac{\int_0^p \theta t \, dt}{\theta/2} = \frac{\theta p^2/2}{\theta/2} = p^2$

556 And thus, substituting in Eq. (A.2), the Gini coefficient of a uniform distribution becomes:

557 (A.8) $GC_X = 1 - 2\int_0^1 p^2 \, dp = 1 - \frac{2}{3} = \frac{1}{3}$

558 Hence, any variable X that has the minimum of zero and is distributed evenly along all its
559 values, such as D or H, would have $GC_X = 0.33$, which thus is the value of Gini Coefficient
560 which corresponds to maximum entropy.

561 ****approximate position of Figure A.1*****

562 *Proofs for the Lorenz curve and Gini Coefficient of the second power of uniformly distributed*
563 *variable*

564 Next, we will proceed to deduce the Lorenz curves $L_{BA}(p)$ and Gini coefficient GC_{BA} values
565 for basal areas that derive from this situation of maximum entropy in the distribution of tree
566 diameters. The basal area is directly calculated from a transformation of the diameters $BA =$
567 aD^2. As per the scale-invariability property of Lorenz curves the scalar a can be further
568 disregarded, and thus we now consider the Lorenz curve and Gini coefficient of transformation
569 $Z = X^2$ when $X \sim U(0, \theta)$.

570 The c.d.f. and p.d.f of the transformed variable are:

571 (A.9) $F_{X^2}(z;\theta) = \begin{cases} 0, & \text{for } z \le 0 \\ \sqrt{z}/\theta, & \text{for } 0 \le z \le \theta^2 \\ 1, & \text{for } z \ge \theta^2 \end{cases}$

572 (A.10) $f_{X^2}(z;\theta) = \begin{cases} \frac{1}{2\theta\sqrt{z}}, & \text{for } 0 \le z \le \theta^2 \\ 0, & \text{otherwise} \end{cases}$

573 Thus, the quantile function and expected value of Z are:

574 (A.11) $F_{X^2}^{-1}(p) = \theta^2 p^2$

575 (A.12) $E[X^2] = \frac{\theta^2}{3}$

576 Substituting these in Eq. (A.1), the Lorenz curve becomes (Figure A.1):

577 (A.13) $L_{X^2}(p) = \frac{\int_0^p \theta^2 t^2 \, dt}{\theta^2/3} = \frac{\theta^2 p^3/3}{\theta^2/3} = p^3$

578 And thus, substituting in Eq. (A.2), the Gini coefficient of a uniform distribution becomes:

579 (A.14) $GC = 1 - 2\int_0^1 p^3 \, dp = 1 - \frac{2}{4} = \frac{1}{2}$

580 Hence, for any variable $Z \propto X^2$ that is proportional to the second power of X, such as of BA

581 is to D, the $GC_{X^2} = 0.50$ corresponds to the maximum entropy of X.

582

583

584

585

586

587

588

589

590

591

592

593

References.

Adnan, S., Maltamo, M., Coomes, D.A., García-Abril, A., Malhi, Y., Manzanera, J.A., Butt, N., Morecroft, M. and Valbuena, R., 2019. A simple approach to forest structure classification using airborne laser scanning that can be adopted across bioregions. Forest Ecology and Management, 433, pp.111-121.

Adnan, S., Maltamo, M., Coomes, D.A. and Valbuena, R., 2017. Effects of plot size, stand density, and scan density on the relationship between airborne laser scanning metrics and the Gini coefficient of tree size inequality. Canadian Journal of Forest Research, 47(12), pp.1590-1602.

Almeida, D.R.A., Stark, S.C., Chazdon, R., Nelson, B.W., César, R.G., Meli, P., Gorgens, E.B., Duarte, M.M., Valbuena, R., Moreno, V.S. and Mendes, A.F., 2019a. The effectiveness of lidar remote sensing for monitoring forest cover attributes and landscape restoration. Forest Ecology and Management, 438, pp.34-43.

Almeida, D.R.A., Stark, S.C., Silva, C.A., Hammamura, C. & Valbuena, R. (2019b) *leafR: a set of functions for analyzing the structure of forests based on the leaf area density (LAD) and leaf area index (LAI) measures calculated from Airborne Laser Scanning (ALS)*. R package. Version 0.3. CRAN - The Comprehensive R Archive Network

Asner, G.P. and Mascaro, J., 2014. Mapping tropical forest carbon: Calibrating plot estimates to a simple LiDAR metric. Remote Sensing of Environment, 140, pp.614-624.

Asner, G.P., Powell, G.V., Mascaro, J., Knapp, D.E., Clark, J.K., Jacobson, J., Kennedy-Bowdoin, T., Balaji, A., Paez-Acosta, G., Victoria, E. and Secada, L., 2010. High-resolution forest carbon stocks and emissions in the Amazon. Proceedings of the National Academy of Sciences, 107(38), pp.16738-16742.

Bakx, T.R., Koma, Z., Seijmonsbergen, A.C. and Kissling, W.D., 2019. Use and categorization of Light Detection and Ranging vegetation metrics in avian diversity and species distribution research. Diversity and distributions, 25(7), pp.1045-1059.

Bollandsås, O.M., and Næsset, E., 2007. Estimating percentile-based diameter distributions in uneven-sized Norway spruce stands using airborne laser scanner data. Scandinavian Journal of Forest Research, 22(1), pp.33-47.

Boudreau, J., Nelson, R.F., Margolis, H.A., Beaudoin, A., Guindon, L. and Kimes, D.S., 2008. Regional aboveground forest biomass using airborne and spaceborne LiDAR in Québec. Remote Sensing of Environment, 112(10), pp.3876-3890.

Bourdier, T., Cordonnier, T., Kunstler, G., Piedallu, C., Lagarrigues, G. and Courbaud, B., 2016. Tree size inequality reduces forest productivity: an analysis combining inventory data for ten European species and a light competition model. PloS one, 11(3), p.e0151852.

Bouvier, M., Durrieu, S., Fournier, R.A. and Renaud, J.P., 2015. Generalizing predictive models of forest inventory attributes using an area-based approach with airborne LiDAR data, Remote Sensing of Environment, 156, pp.322-334.

Brokaw, N.V.L. and Lent, R.A., 1999. Vertical structure. In 'Maintaining Biodiversity in Forest Ecosystems' (Eds I. Hunter and L. Malcom.) pp. 373–399. Cambridge University Press, Cambridge, UK.

Coomes, D.A. and Allen, R.B., 2007. Effects of size, competition and altitude on tree growth. Journal of Ecology, 95(5), pp.1084-1097.

Crespo-Peremarch, P., Fournier, R.A., Nguyen, V.T., van Lier, O.R. and Ruiz, L.Á., 2020. A comparative assessment of the vertical distribution of forest components using full-waveform airborne, discrete airborne and discrete terrestrial laser scanning data. Forest Ecology and Management, 473, p.118268.

Crookston, N.L. and Finley, A.O., 2008. yaImpute: an R package for kNN imputation. Journal of Statistical Software, 23(10), pp.1-16.

Drake, J.B., Knox, R.G., Dubayah, R.O., Clark, D.B., Condit, R., Blair, J.B. and Hofton, M., 2003. Above-ground biomass estimation in closed canopy neotropical forests using lidar remote sensing: Factors affecting the generality of relationships. Global ecology and biogeography, 12(2), pp.147-159.

Erdelen, M., 1984. Bird communities and vegetation structure: I. Correlations and comparisons of simple and diversity indices. Oecologia, 61(2), pp.277-284.

Fahey, R.T., Atkins, J.W., Gough, C.M., Hardiman, B.S., Nave, L.E., Tallant, J.M., Nadehoffer, K.J., Vogel, C., Scheuermann, C.M., Stuart-Haëntjens, E. and Haber, L.T., 2019. Defining a spectrum of integrative trait-based vegetation canopy structural types. Ecology letters, 22(12), pp.2049-2059.

Franklin, J., 1986. Thematic Mapper analysis of coniferous forest structure and composition. International Journal of Remote Sensing, 7(10), pp.1287-1301

Gibbs, H.K., Brown, S., Niles, J.O. and Foley, J.A., 2007. Monitoring and estimating tropical forest carbon stocks: making REDD a reality. Environmental Research Letters, 2(4), p.045023.

Gini, C., 1921. Measurement of inequality of incomes. The Economic Journal, 31(121), pp.124-126.

Gobakken, T. and Næsset, E., 2008. Assessing effects of laser point density, ground sampling intensity, and field sample plot size on biophysical stand properties derived from airborne laser scanner data. Canadian Journal of Forest Research, 38(5), pp.1095-1109.

Görgens E.B., Valbuena R. & Rodríguez L.C., 2017. A Method for Optimizing Height Threshold when Computing Airborne Laser Scanning Metrics. Photogrammetric Engineering and Remote Sensing 83(5), pp.343-350

Häbel, H., Kuronen, M., Henttonen, H.M., Kangas, A. and Myllymäki, M., 2019. The effect of spatial structure of forests on the precision and costs of plot-level forest resource estimation. Forest Ecosystems, 6(1), p.8.

Hagar, J.C., Yost, A. and Haggerty, P.K., 2020. Incorporating LiDAR metrics into a structure-based habitat model for a canopy-dwelling species. Remote Sensing of Environment, 236, p.111499.

671 Hall, S.A., Burke, I.C., Box, D.O., Kaufmann, M.R. and Stoker, J.M., 2005. Estimating stand
672 structure using discrete-return lidar: an example from low density, fire prone ponderosa pine
673 forests. Forest Ecology and Management, 208(1-3), pp.189-209.

674 Hernando, A., Puerto, L., Mola-Yudego, B., Manzanera, J.A., García-Abril, A., Maltamo, M.
675 and Valbuena, R., 2019. Estimation of forest biomass components using airborne LiDAR and
676 multispectral sensors. iForest-Biogeosciences and Forestry, 12(2), p.207.

677 Hudak, A.T., Crookston, N.L., Evans, J.S., Falkowski, M.J., Smith, A.M., Gessler, P.E. and
678 Morgan, P., 2006. Regression modeling and mapping of coniferous forest basal area and tree
679 density from discrete-return lidar and multispectral satellite data. Canadian Journal of Remote
680 Sensing, 32(2), pp.126-138.

681 Jaskierniak, D., Lane, P.N., Robinson, A. and Lucieer, A., 2011. Extracting LiDAR indices to
682 characterise multilayered forest structure using mixture distribution functions. Remote Sensing
683 of Environment, 115(2), pp.573-585.

684 Kankare, V., Vastaranta, M., Holopainen, M., Räty, M., Yu, X., Hyyppä, J., Hyyppä, H., Alho,
685 P. and Viitala, R., 2013. Retrieval of forest aboveground biomass and stem volume with
686 airborne scanning LiDAR. Remote Sensing, 5(5), pp.2257-2274.

687 Knapp, N., Fischer, R., Cazcarra-Bes, V. and Huth, A., 2020. Structure metrics to generalize
688 biomass estimation from lidar across forest types from different continents. Remote Sensing of
689 Environment, 237, p.111597.

690 Koukoulas, S. and Blackburn, G.A., 2005. Mapping individual tree location, height and species
691 in broadleaved deciduous forest using airborne LIDAR and multi-spectral remotely sensed
692 data. International Journal of Remote Sensing, 26(3), pp.431-455.

693 Kronseder, K., Ballhorn, U., Böhm, V. and Siegert, F., 2012. Above ground biomass estimation
694 across forest types at different degradation levels in Central Kalimantan using LiDAR data.
695 International Journal of Applied Earth Observation and Geoinformation, 18, pp.37-48.

696 Lefsky, M.A., Cohen, W.B., Parker, G.G. and Harding, D.J., 2002a. Lidar remote sensing for
697 ecosystem studies: Lidar, an emerging remote sensing technology that directly measures the
698 three-dimensional distribution of plant canopies, can accurately estimate vegetation structural
699 attributes and should be of particular interest to forest, landscape, and global ecologists.
700 BioScience, 52(1), pp.19-30.

701 Lefsky, M.A., Cohen, W.B., Harding, D.J., Parker, G.G., Acker, S.A. and Gower, S.T., 2002b.
702 Lidar remote sensing of above-ground biomass in three biomes. Global ecology and
703 biogeography, 11(5), pp.393-399.

704 Leite, H.G. and Tavares de Oliveira, F.H., 2002. Statistical procedure to test identity between
705 analytical methods. Communications in soil science and plant analysis, 33(7-8), pp.1105-1118.

706 Lexerød, N.L., and Eid, T. 2006. An evaluation of different diameter diversity indices based
707 on criteria related to forest management planning. Forest Ecology and Management, 222, pp.
708 17–28. doi:10.1016/j.foreco.2005.10.046.

Lindenmayer, D.B., Cunningham, R.B., Donnelly, C.F. and Franklin, J.F., 2000. Structural features of old-growth Australian montane ash forests. Forest Ecology and Management, 134(1-3), pp.189-204.

Listopad, C.M.C.S., Masters, R.E., Drake, J., Weishampel, J. and Branquinho, C., 2015. Structural diversity indices based on airborne LiDAR as ecological indicators for managing highly dynamic landscapes. Ecological Indicators, 57. pp.268-279.

Longo, M., Keller M., dos-Santos, M.N., Leitold, V., Pinagé, E.R., Baccini, A., Saatchi, S., Nogueira, L.M., Batistella M. and Morton, D.C., 2017. Aboveground biomass variability across intact and degraded forests in the Brazilian Amazon. Global Biogeochemical Cycles 33. pp.1639

Lovejoy, T. E., 1972. Bird species diversity and composition in Amazonian rain forests. American Zoologist, 12, 711-2.

Lumley, T. and Miller, A., 2017. Leaps: regression subset selection. R package version, 3.0.

Magnussen, S., Eggermont, P. and LaRiccia, V.N., 1999. Recovering tree heights from airborne laser scanner data. Forest science, 45(3), pp.407-422.

Maltamo, M., Mustonen, K., Hyyppä, J., Pitkänen, J. and Yu, X., 2004. The accuracy of estimating individual tree variables with airborne laser scanning in a boreal nature reserve. Canadian Journal of Forest Research, 34(9), pp.1791-1801.

Maltamo, M., Ørka, H.O., Bollandsås, O.M., Gobakken, T., Næsset, E. 2015. Using pre-classification to improve the accuracy of species-specific forest attribute estimates from airborne laser scanner data and aerial images. Scandinavian Journal of Forest Research. 30: 336-345.

Maltamo, M., Packalén, P., Yu, X., Eerikäinen, K., Hyyppä, J. and Pitkänen, J., 2005. Identifying and quantifying structural characteristics of heterogeneous boreal forests using laser scanner data. Forest ecology and management, 216(1-3), pp.41-50.

Mascaro, J., Litton, C.M., Hughes, R.F., Uowolo, A. and Schnitzer, S.A., 2011. Minimizing bias in biomass allometry: model selection and log-transformation of data. Biotropica, 43(6), pp.649-653.

Mehtätalo, L. and Lappi, J. 2020. *Biometry for Forestry and Environmental Data: with examples in R*. New York: Chapman and Hall/CRC.

McArthur, R.H., McArthur, J.W., 1961. On bird species diversity. Ecology 42, 594–598.

McElhinny, C., Gibbons, P., Brack, C. and Bauhus, J., 2005. Forest and woodland stand structural complexity: its definition and measurement. Forest Ecology and Management, 218(1-3), pp.1-24.

McGaughey, R. 2019. FUSION/LDV: software for LIDAR data analysis and visualization. Version 3.70. USDA Forest Service, Pacific Northwest Research Station [accessed December 2018].

746 Mcinerney, D.O., Suarez-Minguez, J., Valbuena, R. and Nieuwenhuis, M., 2010. Forest canopy
747 height retrieval using LiDAR data, medium-resolution satellite imagery and k NN estimation
748 in Aberfoyle, Scotland. Forestry, 83(2), pp.195-206.

749 Mehtätalo, L. and Nyblom, J., 2009. Estimating forest attributes using observations of canopy
750 height: a model-based approach. Forest Science, 55(5), pp.411-422.

751 Mehtätalo, L. and Nyblom, J., 2012. A Model-Based Approach for Airborne Laser Scanning
752 Inventory: Application for Square Grid Spatial Pattern. Forest Science, 58(2), pp.106-118.

753 Moran, C.J., Rowell, E.M. and Seielstad, C.A., 2018. A data-driven framework to identify and
754 compare forest structure classes using LiDAR. Remote Sensing of Environment, 211, pp.154-
755 166.

756 Mononen, L., Auvinen, A.P., Packalen, P., Virkkala, R., Valbuena, R., Bohlin, I., Valkama, J.
757 and Vihervaara, P., 2018. Usability of citizen science observations together with airborne laser
758 scanning data in determining the habitat preferences of forest birds. Forest Ecology and
759 Management, 430, pp.498-508.

760 Næsset, E., 2002. Predicting forest stand characteristics with airborne scanning laser using a
761 practical two-stage procedure and field data. Remote sensing of environment, 80(1), pp.88-99.

762 Næsset, E. and Gobakken, T., 2008. Estimation of above-and below-ground biomass across
763 regions of the boreal forest zone using airborne laser. Remote Sensing of Environment, 112(6),
764 pp.3079-3090.

765 Näslund, M., 1936. Skogsförsöksanstaltens gallringsförsök i tallskog. Meddelanden från
766 Statens Skogsförsöksanstalt 29. p.169.

767 Neumann, M. and Starlinger, F., 2001. The significance of different indices for stand structure
768 and diversity in forests. Forest ecology and Management, 145(1-2), pp.91-106.

769 Papa, D.A, de Almeida, D.R.A., Silva, C.A., Figueiredo, E.O., Stark, S.C., Valbuena, R.,
770 Rodriguez, L.C.E. and d'Oliveira, M.V.N., 2020. Evaluating tropical forest classification and
771 field sampling stratification from lidar to reduce effort and enable landscape monitoring. Forest
772 Ecology and Management, 457, p.117634.

773 Piñeiro, G., Perelman, S., Guerschman, J.P. and Paruelo, J.M., 2008. How to evaluate models:
774 observed vs. predicted or predicted vs. observed?. Ecological Modelling, 216(3-4), pp.316-
775 322.

776 Pearson, D.L., 1975. The relation of foliage complexity to ecological diversity of three
777 Amazonian bird communities. The Condor, 77(4), pp.453-466.

778 R Core Team. 2019. R: a language and environment for statistical computing [online]. R
779 Foundation for Statistical Computing, Vienna, Austria. Available from http://www.R-
780 project.org.

781 Räty, J., Packalen, P. and Maltamo, M., 2018. Comparing nearest neighbor configurations in
782 the prediction of species-specific diameter distributions. Annals of forest science, 75(1), p.26.

783 Repola, J., 2008. Biomass equations for birch in Finland. Silva Fennica, 42(1): 605-624.

784 Repola, J., 2009. Biomass equations for Scots pine and Norway spruce in Finland. Silva
785 Fennica 43(4): 625-647.

786 Ruiz, L.A., Hermosilla, T., Mauro, F., and Godino, M. 2014. Analysis of the influence of plot
787 size and LiDAR density on forest structure attribute estimates. Forests, 5(5): 936–951.
788 doi:10.3390/f5050936.

789 Schneider, F.D., Morsdorf, F., Schmid, B., Petchey, O.L., Hueni, A., Schimel, D.S. and
790 Schaepman, M.E., 2017. Mapping functional diversity from remotely sensed morphological
791 and physiological forest traits. Nature communications, 8(1), pp.1-12.

792 Shannon, C. E. 1948. A mathematical theory of communication. The Bell System Technical
793 Journal, 27, pp.379–423 and 623–656.

794 Siipilehto J., 1999. Improving the accuracy of predicted basal-area diameter distribution in
795 advanced stands by determining stem number. Silva Fenn 33.

796 Simonson, W.D., Allen, H.D. and Coomes, D.A., 2014. Applications of airborne lidar for the
797 assessment of animal species diversity. Methods in Ecology and Evolution, 5(8), pp.719-729.

798 Stark, S.C., Leitold, V., Wu, J.L., Hunter, M.O., de Castilho, C.V., Costa, F.R., McMahon,
799 S.M., Parker, G.G., Shimabukuro, M.T., Lefsky, M.A. and Keller, M., 2012. Amazon forest
800 carbon dynamics predicted by profiles of canopy leaf area and light environment. Ecology
801 letters, 15(12), pp.1406-1414.

802 Straub, C., Tian, J., Seitz, R. and Reinartz, P., 2013. Assessment of Cartosat-1 and WorldView-
803 2 stereo imagery in combination with a LiDAR-DTM for timber volume estimation in a highly
804 structured forest in Germany. Forestry, 86(4), pp.463-473.

805 Sung, P.Y., and Bera, A.K., 2009. "Maximum entropy autoregressive conditional
806 heteroskedasticity model". Journal of Econometrics. 150 (2): 219–230. CiteSeerX
807 10.1.1.511.9750. doi:10.1016/j.jeconom.2008.12.014.

808 Valbuena, R., Packalen, P., Mehtätalo, L., García-Abril, A. and Maltamo, M., 2013.
809 Characterizing forest structural types and shelterwood dynamics from Lorenz-based indicators
810 predicted by airborne laser scanning. Canadian journal of forest research, 43(11), pp.1063-
811 1074.

812 Valbuena, R., Packalén, P., Martín, S. and Maltamo, M., 2012. Diversity and equitability
813 ordering profiles applied to study forest structure. Forest Ecology and Management, 276,
814 pp.185-195.

815 Valbuena, R., Maltamo, M. and Packalen, P., 2016. Classification of multilayered forest
816 development classes from low-density national airborne lidar datasets. Forestry: An
817 International Journal of Forest Research, 89(4), pp.392-401.

818 Valbuena, R., Maltamo, M., Mehtätalo, L. and Packalen, P., 2017a. Key structural features of
819 boreal forests may be detected directly using L-moments from airborne lidar data. Remote
820 Sensing of Environment, 194, pp.437-446.

821 Valbuena, R., Hernando, A., Manzanera, J.A., Görgens, E.B., Almeida, D.R.A., Mauro, F.,
822 García-Abril, A. and Coomes, D.A., 2017b. Enhancing of accuracy assessment for forest

above-ground biomass estimates obtained from remote sensing via hypothesis testing and overfitting evaluation. Ecological Modelling, 366, pp.15-26.

Valbuena, R., O'Connor, B., Zellweger, F., Simonson, W., Vihervaara, P., Maltamo, M., Silva, C.A., Almeida, D.R.A., Danks, F., Morsdorf, F. and Chirici, G., 2020. Standardizing Ecosystem Morphological Traits from 3D Information Sources. Trends in Ecology & Evolution [in press].

Van Aardt, J.A., Wynne, R.H. and Scrivani, J.A., 2008. Lidar-based mapping of forest volume and biomass by taxonomic group using structurally homogenous segments. Photogrammetric Engineering & Remote Sensing, 74(8), pp.1033-1044.

Vierling, K.T., Vierling, L.A., Gould, W.A., Martinuzzi, S. and Clawges, R.M., 2008. Lidar: shedding new light on habitat characterization and modeling. Frontiers in Ecology and the Environment, 6(2), pp.90-98.

Vincent, G., Sabatier, D. and Rutishauser, E., 2014. Revisiting a universal airborne light detection and ranging approach for tropical forest carbon mapping: scaling-up from tree to stand to landscape. Oecologia, 175(2), pp.439-443.

Weiner, J. and Thomas, S.C., 1986. Size variability and competition in plant monocultures. Oikos, pp.211-222.

Weisberg, P.J., Dilts, T.E., Becker, M.E., Young, J.S., Wong-Kone, D.C., Newton, W.E. and Ammon, E.M., 2014. Guild-specific responses of avian species richness to lidar-derived habitat heterogeneity. Acta oecologica, 59, pp.72-83.

Wilkes, P., Jones, S.D., Suarez, L., Haywood, A., Mellor, A., Woodgate, W., Soto-Berelov, M. and Skidmore, A.K., 2016. Using discrete-return airborne laser scanning to quantify number of canopy strata across diverse forest types. Methods in ecology and evolution, 7(6), pp.700-712.

Zolkos, S.G., Goetz, S.J. and Dubayah, R., 2013. A meta-analysis of terrestrial aboveground biomass estimation using lidar remote sensing. Remote Sensing of Environment, 128, pp.289-298.

Tables

Table 1. Aboveground biomass and other forest attributes calculated at each forest development class.

Development Class			AGB (Mg·ha^{-1})	QMD (cm)	GC_{BA}	N (trees·ha^{-1})	GC_H / L_{cv}	L_{skew}
	Seedlings	Min	2.48	0.10	0.00	13909	0.07	0.14
		Mean	**7.96**	**0.10**	**0.00**	**44770**	**0.23**	**0.31**
		Max	28.51	0.10	0.00	182522	0.54	0.70
		SD	5.14	0.00	0.00	32987	0.09	0.13
	Saplings	Min	6.14	0.10	0.00	1601	0.20	-0.18
		Mean	**34.88**	**3.05**	**0.35**	**31852**	**0.42**	**0.21**
		Max	112.48	6.93	0.89	110774	0.60	0.59
		SD	24.62	1.78	0.29	24754	0.12	0.20
	Young	Min	13.09	6.23	0.25	864	0.15	-0.36
		Mean	**79.91**	**10.00**	**0.43**	**3254**	**0.29**	**-0.11**
		Max	160.01	14.44	0.66	6523	0.58	0.33
		SD	31.67	2.18	0.09	1475	0.11	0.17
	Advanced	Min	49.56	12.68	0.15	314	0.09	-0.41
		Mean	**96.98**	**17.27**	**0.42**	**1003**	**0.28**	**-0.20**
		Max	182.76	22.15	0.63	2082	0.50	0.14
		SD	30.26	2.63	0.14	462	0.10	0.13
	Mature	Min	73.75	16.07	0.19	314	0.09	-0.48
		Mean	**179.07**	**23.35**	**0.49**	**844**	**0.23**	**-0.21**
		Max	410.55	32.44	0.68	1807	0.41	0.00
		SD	76.81	4.60	0.17	374	0.08	0.11
	Shelterwood	Min	23.15	3.32	0.79	9020	0.21	-0.36
		Mean	**171.01**	**5.63**	**0.95**	**33935**	**0.36**	**0.07**
		Max	305.34	9.25	1.00	108805	0.57	0.26
		SD	83.39	1.65	0.06	24028	0.10	0.15
	Seed Trees	Min	23.65	2.29	0.11	117	0.14	-0.23
		Mean	**70.43**	**14.76**	**0.73**	**9833**	**0.58**	**0.37**
		Max	143.52	38.14	0.99	39601	0.85	0.90
		SD	28.29	12.14	0.35	11209	0.21	0.31
	Multi-Storied	Min	17.99	1.41	0.68	2219	0.20	-0.22
		Mean	**77.02**	**3.87**	**0.92**	**33279**	**0.58**	**0.30**
		Max	271.39	9.60	0.99	78131	0.84	0.83
		SD	54.73	2.19	0.09	16382	0.16	0.30

AGB: aboveground biomass; QMD: quadratic mean diameter; GC_{BA}: Gini coefficient of basal area; GC_H: Gini coefficient of LiDAR; L_{cv}: L-coefficient of variation of LiDAR heights; L_{skew}: L-skewness of LiDAR heights SD: standard deviation

865 **Table 2.** Airborne LiDAR predictors selection (best subset) for the general model (whole data
866 without pre-stratification) and each forest structural type specific model (even sized, uneven
867 sized, oligophotic/closed canopy and euphotic/open canopy forest structures).

Predictors	General Model	GC_H (L_{cv})		L_{skew}	
		Even (<0.33)	Uneven (>0.33)	Oligophotic (<0)	Euphotic (>0)
Variance	*		*		*
Median of the absolute deviations (MAD) from the overall mode	*	*		*	
MAD from the overall median					*
L.skewness		*			
Average absolute deviation (AAD)			*		
Cubic mean					*
Quadratic mean		*			
25th height percentile	*				
50th height percentile	*	*		*	
60th height percentile					*
70th height percentile			*		
99th height percentile			*		*
% first returns above 0.1m			*		
% all returns above 0.1 m				*	
% all returns above mean				*	
% first returns above mode		*		*	
Ratio returns above 0.1 m / total first returns	*	*	*		*
Canopy relief ratio	*			*	

868

869

870 **Table 3.** Accuracy assessment of the observed and predicted aboveground biomass of the
871 general model.

	Whole Data	GC_H (L_{cv})		L_{skew}	
		Even (<0.33)	Uneven (>0.33)	Oligophotic (<0)	Euphotic (>0)
Sample size	**244**	**120**	**124**	**119**	**125**
MD	-3.55	-2.09	-4.97	-4.56	-4.31
MD (%)	-3.95	-2.33	-5.54	-5.08	-4.81
RMSD	37.4	37.1	37.6	37.6	37.3
RMSD (%)	41.7	41.4	41.9	41.9	41.6
SSR	1.03	1.02	1.04	1.04	0.98

872 $GC_H(L_{cv})$: Gini coefficient/L-coefficient of variation of LiDAR heights; L_{skew}: L-skewness of
873 LiDAR heights; MD: mean difference; RMSD: relative mean square difference;.

874

875

Table 4. Accuracy assessment of the observed and predicted aboveground biomass of each forest structural type specific models.

(a) Even versus uneven-sized structure

	Whole Data	GC_H (L_{cv})	
		Even (<0.33)	Uneven (>0.33)
Sample size	**244**	**120**	**124**
MD	-2.52	-2.30	-2.72
MD (%)	-2.81	-2.57	-3.03
RMSD	34.9	34.6	35.3
RMSD (%)	38.9	38.6	39.4
SSR	0.97	0.96	0.99

(b) Oligophotic/closed canopy versus euphotic/open canopy areas

	Whole Data	L_{skew}	
		Oligophotic (<0)	Euphotic (>0)
Sample size	**244**	**119**	**125**
MD	-2.37	-2.22	-2.52
MD (%)	-2.64	-2.48	-2.81
RMSD	33.2	33.5	32.9
RMSD (%)	37.0	37.4	36.7
SSR	0.98	0.98	0.98

$GC_H(L_{cv})$: Gini coefficient/L-coefficient of variation of LiDAR heights; L_{skew}: L-skewness of LiDAR heights; MD: mean difference; RMSD: relative mean square difference; SSR: sum of square ratio.

Figure Captions

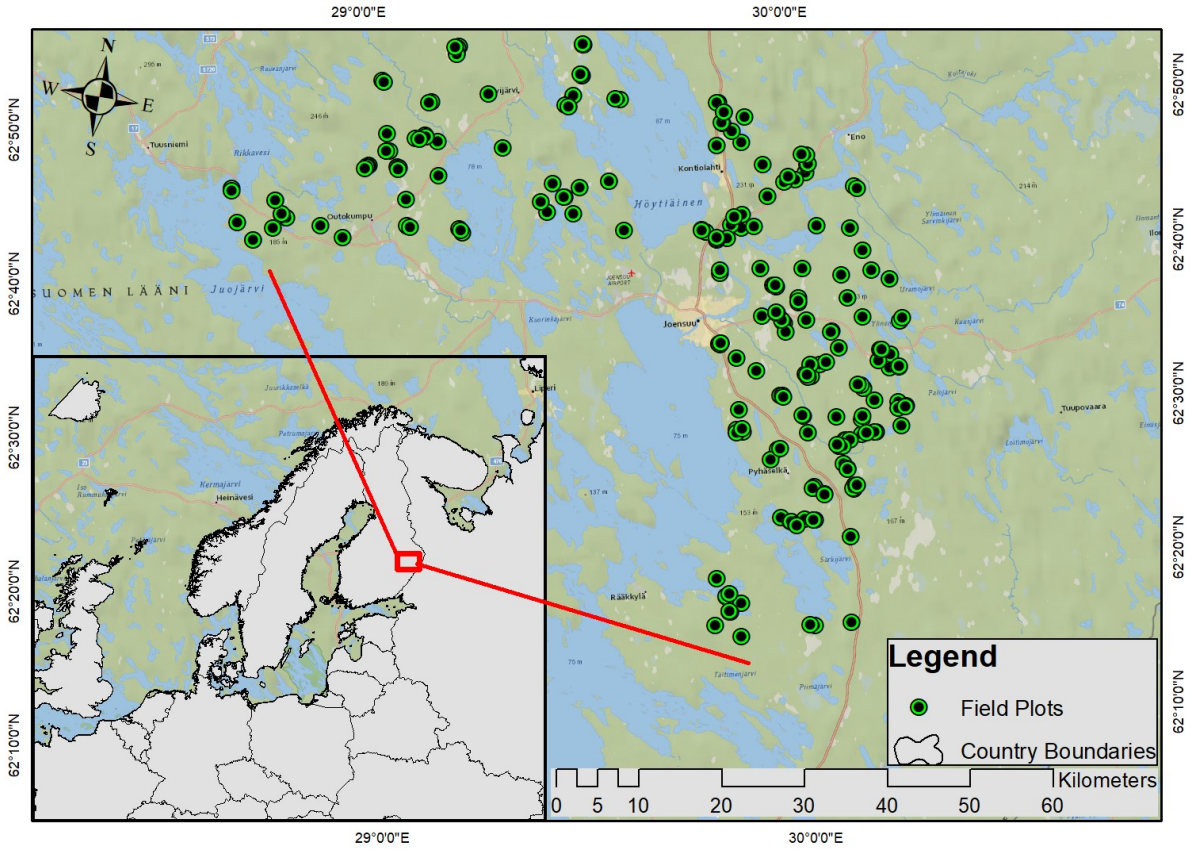

Figure 1. Map of the North Karelia Region, Finland (study area).

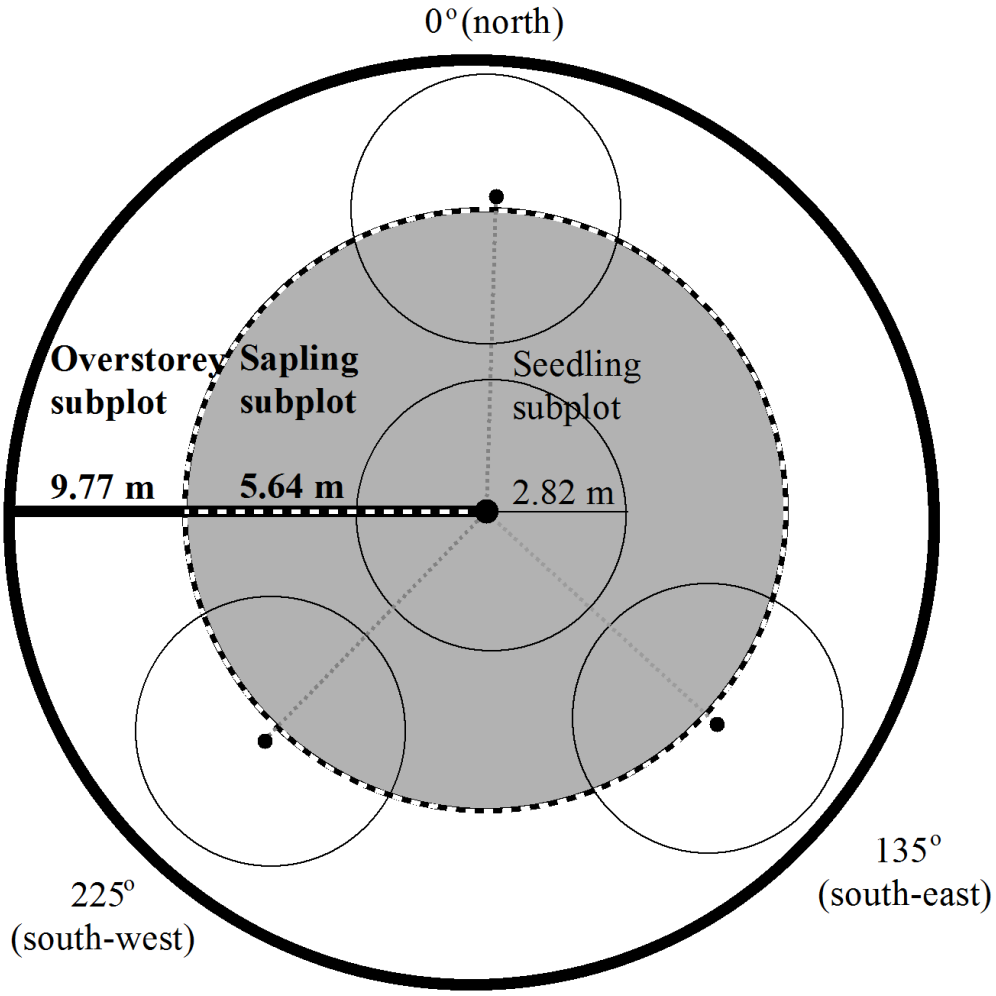

912
913 **Figure 2.** Plot design for field data collection.
914
915
916
917
918
919
920
921
922
923

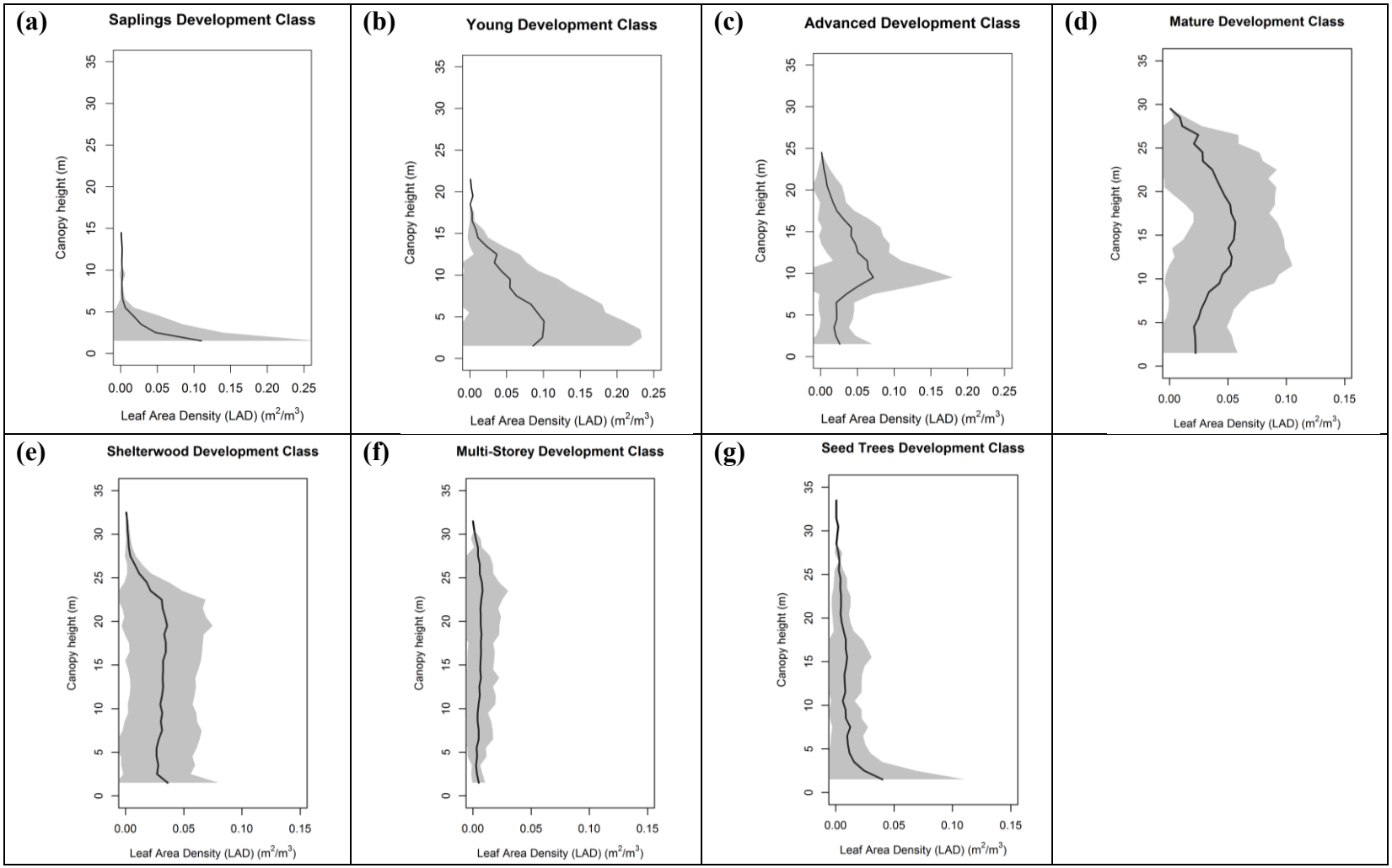

924 **Figure 3.** Mean leaf area density (LAD) profiles calculated directly from LiDAR data for each development class (a) Sapling (b) Young (c)
925 Advanced (d) Mature (e) Shelterwood (f) Multi-storey and (g) Seed trees. Lines show mean LAD of all plots and grey areas their 95%
926 confidence intervals.

927

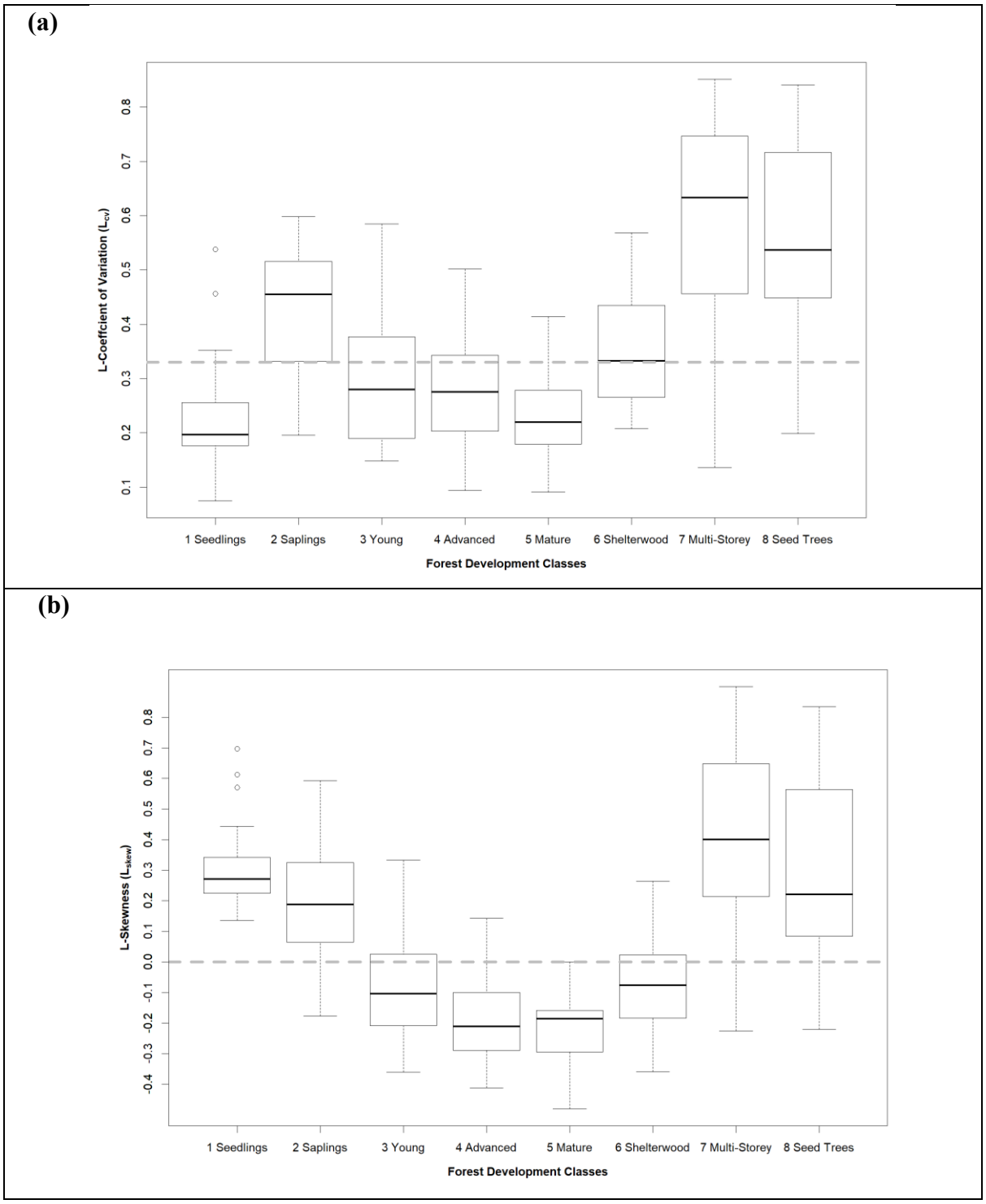

928

929 **Figure 4**. Distribution of different forest development classes on either side of the (a)

930 $L_{cv}(GC_H) = 0.33$ and (b) $L_{skew} = 0$.

931

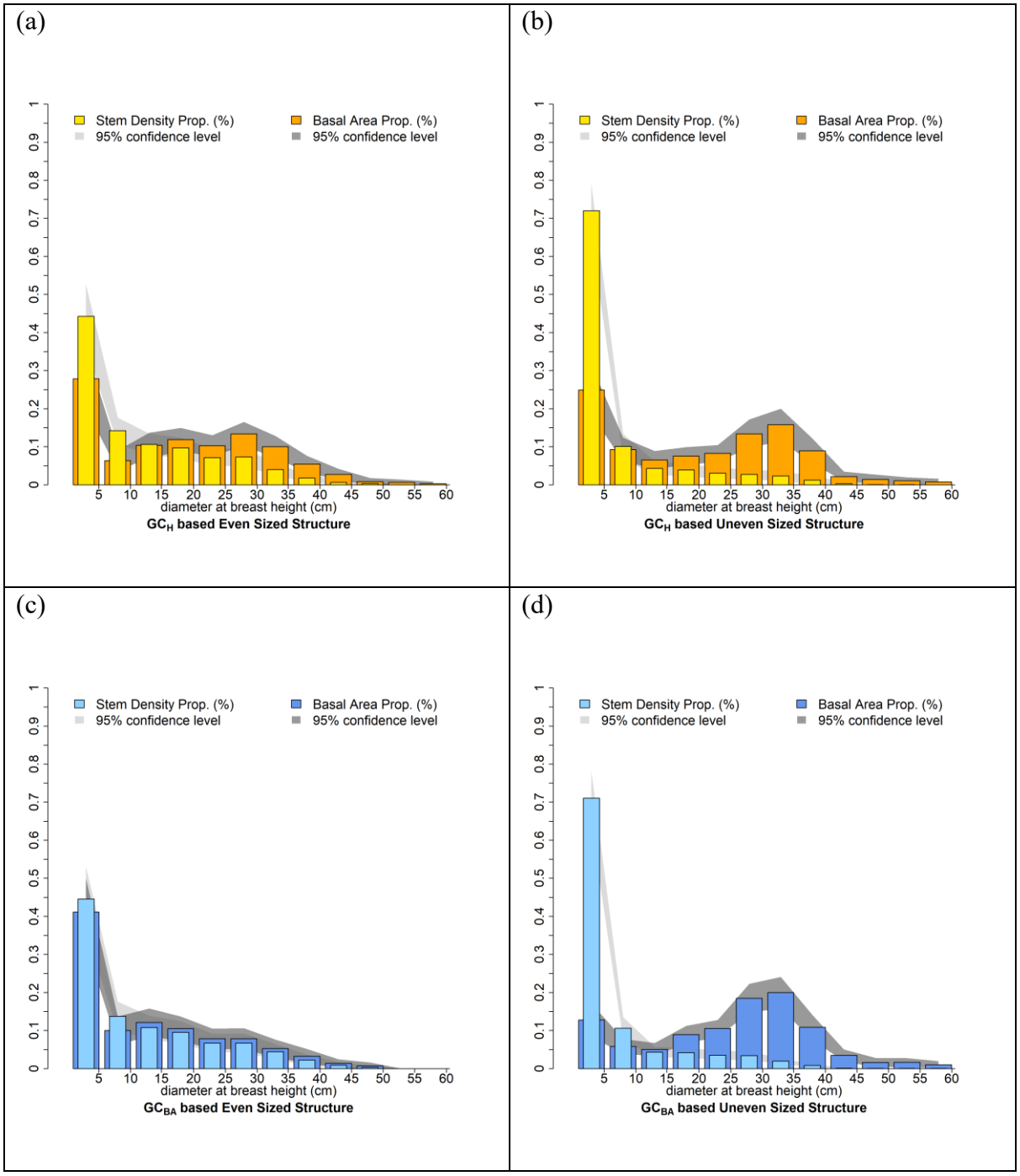

932

933

934 **Figure 5**. Comparison of diameter and basal area distribution in the even and uneven sized

935 forest structural types separated by Gini coefficient of LiDAR ($GC_H(L_{cv}) = 0.33$) (a, b) and

936 Gini coefficient of basal area ($GC_{BA} = 0.5$) (c, d).

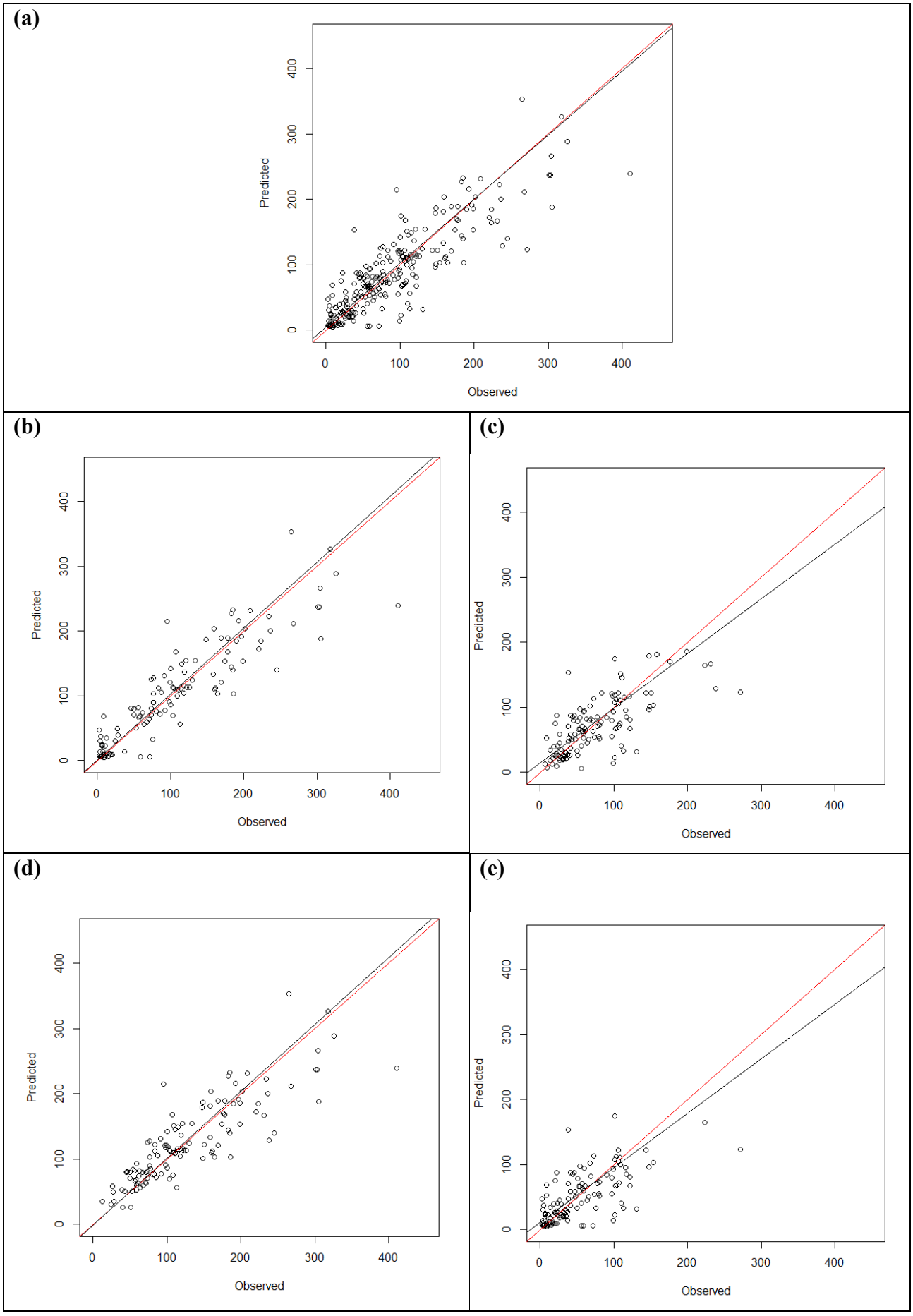
(a)
Predicted
Observed
0
100
200
300
400
(b)
Predicted
Observed
0
100
200
300
400
(c)
Predicted
Observed
0
100
200
300
400
(d)
Predicted
Observed
0
100
200
300
400
(e)
Predicted
Observed
0
100
200
300
400

Figure 6. Observed vs predicted aboveground biomass ($Mg \cdot ha^{-1}$) plots of the kNN imputation method using general model for (a) whole data without pre-stratification and each forest structural types obtained directly from airborne LiDAR classification such as (b) even sized, (c) uneven sized, (d) oligophotic/closed canopy and (e) euphotic/open canopy. The red line represents 1:1 correspondence and the black line shows linear regression fit between observed and predicted values.

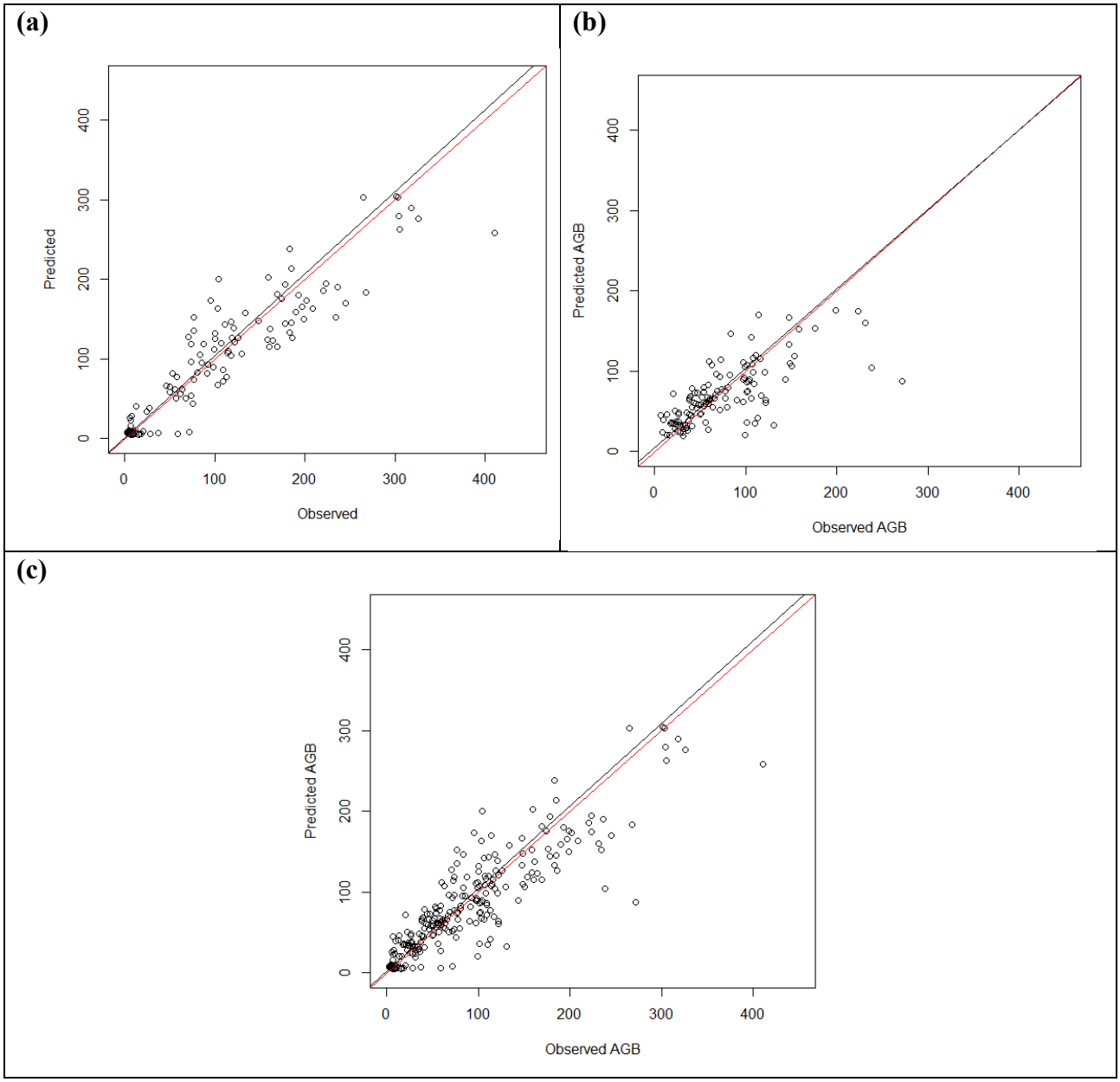

951

952 **Figure 7**. Observed vs predicted aboveground biomass ($Mg \cdot ha^{-1}$) plots of the kNN imputation
953 method using specific models developed for (a) even sized and (b) uneven sized forest structure
954 and their combination for the (c) whole data. The red line represents 1:1 correspondence and
955 the black line shows linear regression fit between observed and predicted values.

956

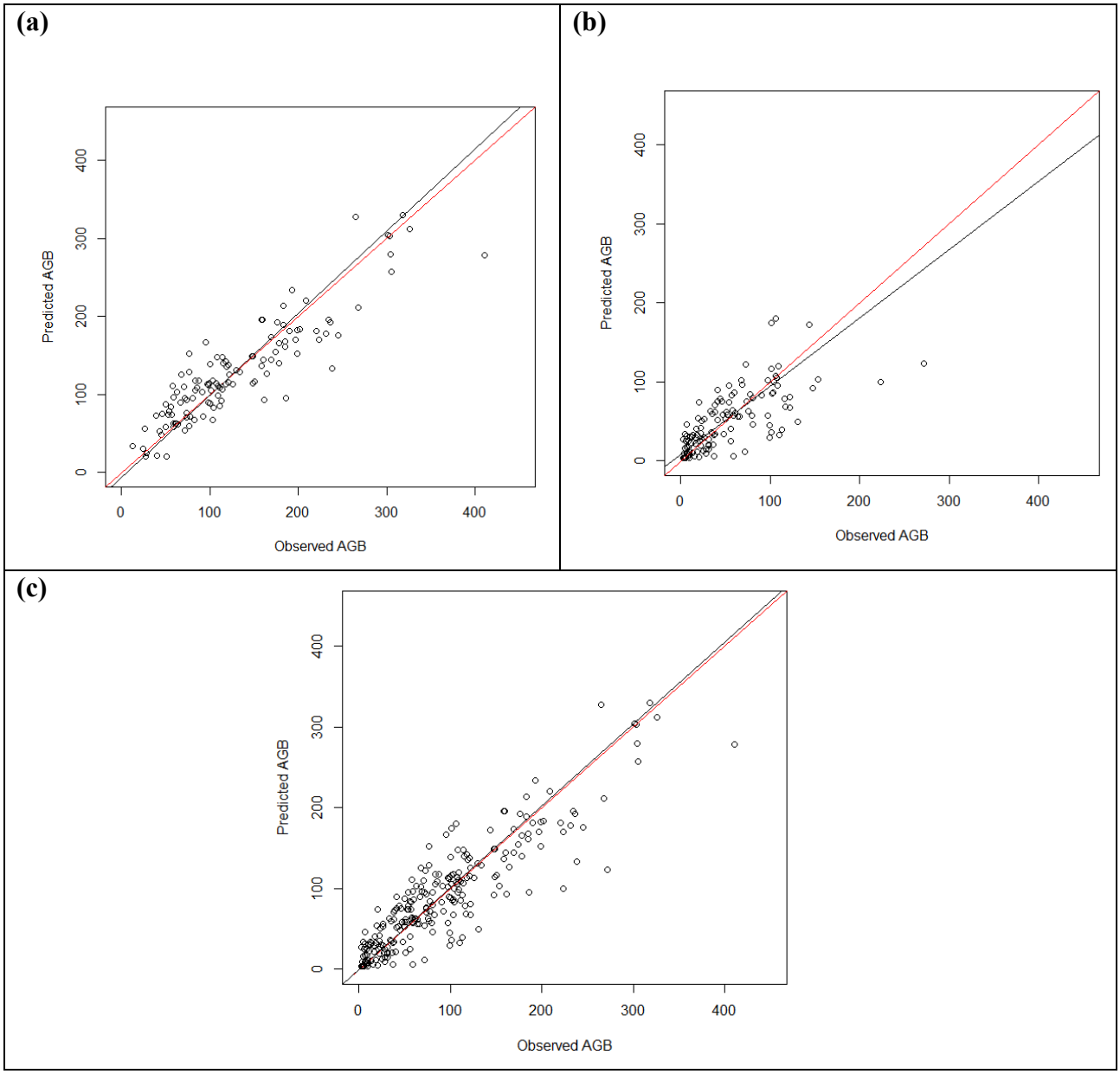

957

958 **Figure 8**. Observed vs predicted aboveground biomass ($Mg \cdot ha^{-1}$) plots of the kNN imputation
959 method using specific models for (a) oligophotic areas/closed canopies and (b) euphotic
960 areas/open canopies and their combination for the (c) whole data. The red line represents 1:1
961 correspondence and the black line shows linear regression fit between observed and predicted
962 values.

963

964

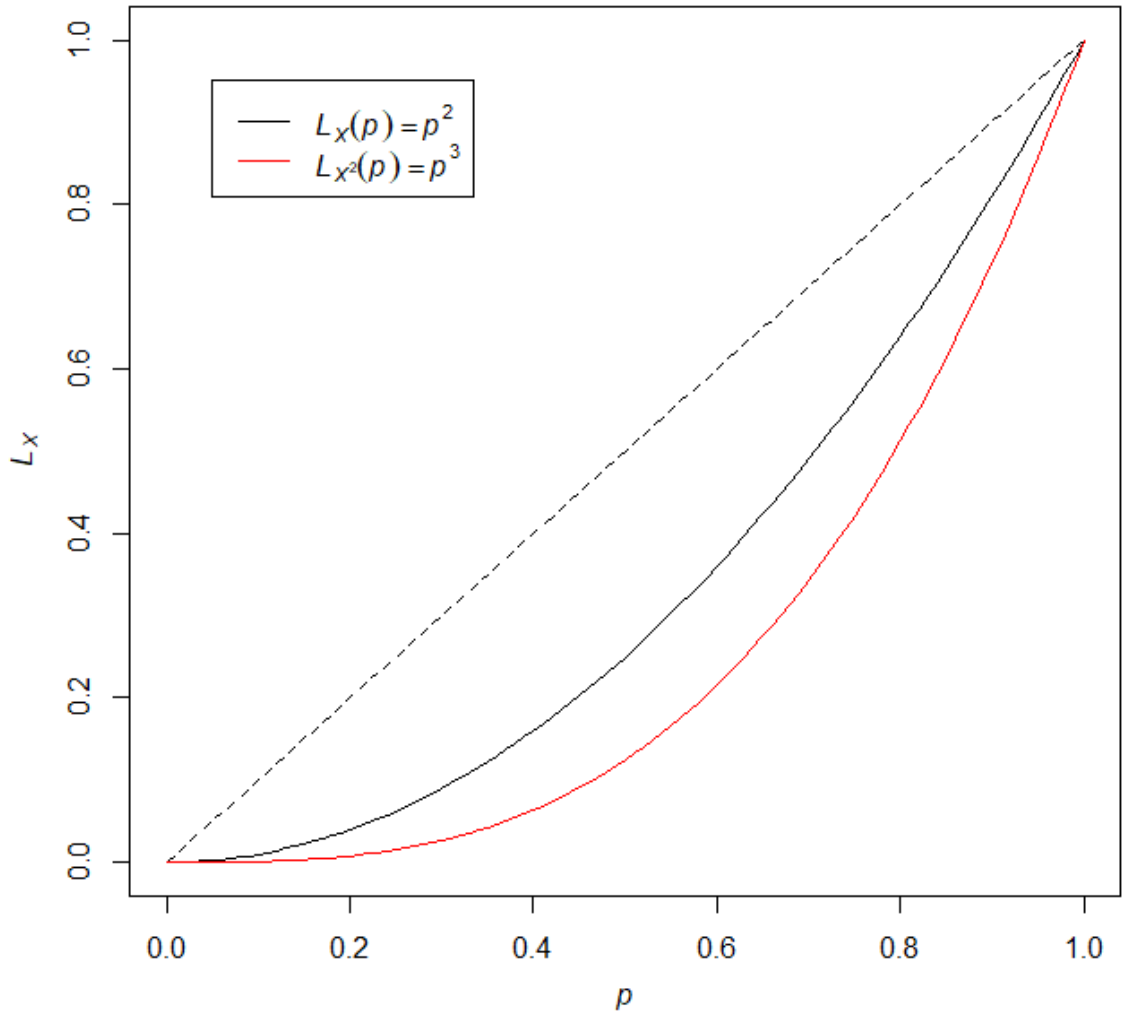

965

966 **Figure A1**. Lorenz curves of maximum entropy for X, and its transformed variable $Z \propto X^2$.